

The physics discussed so far is generic. The materials presented in Chapters 3–6 not only apply to GRBs, but also apply to any high-energy astrophysical phenomena invoking relativistic shocks and non-thermal particles. Starting from this chapter, we will apply the physics to GRBs.

With abundant multi-wavelength data collected over the years (Chapter 2), one may say a lot about our understanding of GRBs. However, if one is asked “What do we really know about GRBs?”, the items one might list are limited. The following five items may be said for certain:

- Since they are at cosmological distances, GRBs have huge energies, and, more importantly, the highest isotropic luminosities in the universe. Any model for interpreting GRBs has to meet this *energetics* criterion;
- GRB ejecta must be moving towards Earth with a *relativistic* speed (see §7.1 for a detailed discussion);
- There are at least *two physically distinct categories*, i.e. those associated with deaths of massive stars and those not;
- GRB ejecta are geometrically *beamed*;
- The afterglow emission of at least some (probably most) GRBs is produced due to synchrotron radiation of electrons in the *external shocks* as the ejecta is decelerated by a circumburst medium.

Many aspects of the GRB problem remain *open questions* (e.g. Zhang 2011 for a detailed discussion). The following items are some examples:

- What is the *composition* of the GRB jets?
- What is (are) the *energy dissipation mechanism(s)* in GRB jets that convert(s) energy from other forms to radiation?
- What is (are) the *particle acceleration mechanism(s)* in the GRB prompt emission site?
- What is (are) the *radiation mechanism(s)* of the GRB prompt emission?
- Besides synchrotron radiation from the external shocks, are there other emission processes that give rise to the observed *afterglow*?
- What is the *central engine* of GRBs? Are there different types of central engines (e.g. hyper-accreting black holes vs. millisecond magnetars)?
- What are the *progenitors* of long and short GRBs? Are there more than two types of progenitors?

- Are GRBs bright emitters of non-electromagnetic signals, such as high-energy neutrinos, gravitational waves, and ultra-high-energy cosmic rays?
- Are long GRBs unbiased tracers of the star formation history of the universe?
- Can population III stars make GRBs?

These problems will be addressed in the later chapters of the book. This chapter aims at laying out a *basic theoretical framework* for understanding GRBs. Without getting into the details of the central engine and progenitor, a generic *energy flow* in the GRB problem is highlighted. This includes what may be the initial forms of energy at the central engine and how energy in different forms gets converted to non-thermal particle energy during the evolution of the jet and eventually released as the radiation energy we receive. The chapter starts with various theoretical arguments and observational evidence that GRB ejecta are moving towards Earth with a relativistic speed (§7.1), which is the key ingredient of all GRB models. A *general theoretical framework* of GRBs is introduced in §7.2, which is followed by a discussion on the dynamical evolution of the relativistic jets in different regimes: a matter-dominated fireball (§7.3), a Poynting-flux-dominated outflow (§7.4), and a hybrid outflow (§7.5). A scale model imagining a GRB occurring in the solar system is introduced in §7.6, which helps to clarify the global picture of GRB jet evolution. Finally, several alternative ideas are briefly introduced in §7.7, with some critical comments.

## 7.1 Relativistic Motion

### 7.1.1 Compactness Problem and Solution

One robust argument that GRBs must move relativistically towards Earth is the apparent *compactness problem*, as first discussed by Ruderman (1975).

The problem is the following: we detect photons from GRBs with energy higher than the electron rest mass energy. These photons could have been converted to electron–positron pairs. In order to escape from the GRB source, these photons must have an optical depth for two-photon *pair production* ( $\gamma\gamma \rightarrow e^+e^-$ ) less than unity. However, without relativistic motion, these optical depths greatly exceed unity.

This argument can be elaborated as follows. Since near the threshold the pair production cross section is close to the Thomson cross section  $\sigma_T$  (§5.4.1), to order of magnitude, one may estimate the pair production optical depth as

$$\tau_{\gamma\gamma} \sim \sigma_T n_{\text{ph}} R, \quad (7.1)$$

where  $n_{\text{ph}}$  is the target photon number density, and  $R$  is the size of the emission region. For simplicity, we just consider photons with energy  $\sim m_e c^2$ , so that the considered photons and the target photons have the same energy. In astrophysics, usually the size of an optically thin object can be estimated by its variability time scale  $\delta t$ , so that  $R \sim c\delta t$ . This is based on the consideration that an instantaneous signal emitted everywhere from the source would arrive at the observer with a spread in the arrival time of order  $\delta t = R/c$  due to the

propagation delay of photons from the far end with respect to the near end of the object to the observer.

Let us consider a typical GRB with an observed  $\gamma$ -ray fluence

$$S_\gamma \sim 10^{-6} \text{ erg cm}^{-2}, \quad (7.2)$$

located at a luminosity distance

$$D_L \sim 2 \times 10^{28} \text{ cm}, \quad (7.3)$$

which corresponds to a redshift  $z \sim 1$ . The total “isotropic” energy in the “fireball” is therefore (Eq. (2.49), with the  $k$ -correction factor taken as  $k = 1$  for an order-of-magnitude estimate)

$$E_{\gamma,\text{iso}} \sim 4\pi D_L^2 (1+z)^{-1} S_\gamma \sim 2.5 \times 10^{51} \text{ erg}. \quad (7.4)$$

We take a minimum variability time scale  $\delta t \sim 10$  ms, so that the typical size of the emission region is

$$R \sim c\delta t \sim 3 \times 10^8 \text{ cm}. \quad (7.5)$$

Assuming that a fraction  $f$  of the emitted energy is above the pair threshold  $\epsilon_\gamma \gtrsim m_e c^2$ , then the number density of pair-producing photons is roughly

$$n_{\text{ph}} \sim \frac{3E_{\gamma,\text{iso}}f}{4\pi R^3 \epsilon_\gamma} \sim (2.7 \times 10^{31} \text{ cm}^{-3})f. \quad (7.6)$$

The  $\gamma\gamma$  optical depth (7.1) is therefore

$$\tau_{\gamma\gamma} \sim \frac{3E_{\gamma,\text{iso}}\sigma_{\text{T}}f}{4\pi R^2 \epsilon_\gamma} \sim 5.4 \times 10^{15} f \gg 1, \quad (7.7)$$

so that  $>\text{MeV}$  photons cannot escape from the source and should not have been observed.

To solve this compactness problem, one needs to introduce relativistic motion. If the GRB outflow is moving towards the observer with a Lorentz factor  $\Gamma$  (hereafter capital  $\Gamma$  will be adopted to denote bulk motion), one can identify two effects that help to reduce the  $\gamma\gamma$  opacity.

The first effect is the *effective increase of the threshold energy* in the observer frame, or, equivalently, the *Doppler de-boost* of the photon energy in the comoving frame. For an *on-beam* relativistic outflow (i.e. the outflow aiming squarely towards Earth), in the observer frame, the pair production threshold condition is

$$h\nu_1 \cdot h\nu_2 \geq \Gamma^2 (m_e c^2)^2. \quad (7.8)$$

Compared with the general condition Eq. (5.167), there is a  $\Gamma^2$  factor on the right hand side. This is because Eq. (5.167) applies in the comoving frame, i.e.  $h\nu'_1 \cdot h\nu'_2 \geq (m_e c^2)^2$ , with  $\nu'_1 = \nu_1/\Gamma$  and  $\nu'_2 = \nu_2/\Gamma$  (for on-beam sources, the Doppler factor  $\mathcal{D} \sim \Gamma$ ). This condition greatly eases the escape condition for  $\gamma$ -rays. Effectively, this raises the pair production threshold energy by a factor of  $\Gamma$ . Another way to view this is that, in the comoving frame, all the photons are de-boosted by a factor of  $\Gamma$ . A large fraction of previous “ $\gamma$ -rays” ( $\gtrsim \text{MeV}$ ) above the pair production threshold are now “X-rays” ( $\sim 10$  keV), which are below the threshold.

This effect can be quantified as follows. Assuming a power-law photon number spectrum  $N(\epsilon) \propto \epsilon^\beta$ , with  $\beta \sim -2.2$  (typical value of Band-function spectrum above the peak energy  $E_p$ ), let us consider the number of photons that can annihilate a photon with the same observed energy  $\epsilon_{\text{obs}}$  for both the non-relativistic (NR) and relativistic (R) bulk motion. Suppose for the non-relativistic case the threshold energy is  $\epsilon_{\text{th,NR}}$ . According to Eq. (7.8), the threshold for the relativistic case is larger by a factor of  $\Gamma^2$ , i.e.  $\epsilon_{\text{th,R}} = \Gamma^2 \epsilon_{\text{th,NR}}$ . The ratio between the total number of photons above the two threshold energies, which is also the ratio of the fraction of photons above threshold, is

$$\frac{N(>\epsilon_{\text{th,R}})}{N(>\epsilon_{\text{th,NR}})} = \frac{f_{\text{R}}}{f_{\text{NR}}} = \frac{N_0(\Gamma^2 \epsilon_{\text{th,NR}})^{\beta+1}}{N_0 \epsilon_{\text{th,NR}}^{\beta+1}} = \Gamma^{2\beta+2}. \quad (7.9)$$

The second effect is an *increase in the size of the emission region*. As discussed in §3.2.2, the observed time is smaller than the emission time by a factor of  $\sim \Gamma^2$ . As a result, the inferred emission region size using the observed variability time scale should be scaled up by a factor  $\Gamma^2$  in the lab frame, i.e.

$$\frac{R_{\text{R}}}{R_{\text{NR}}} = \Gamma^2. \quad (7.10)$$

Noticing Eq. (7.7), one can then use Eqs. (7.9) and (7.10) to derive the ratio of the pair production optical depth for the relativistic and non-relativistic cases:<sup>1</sup>

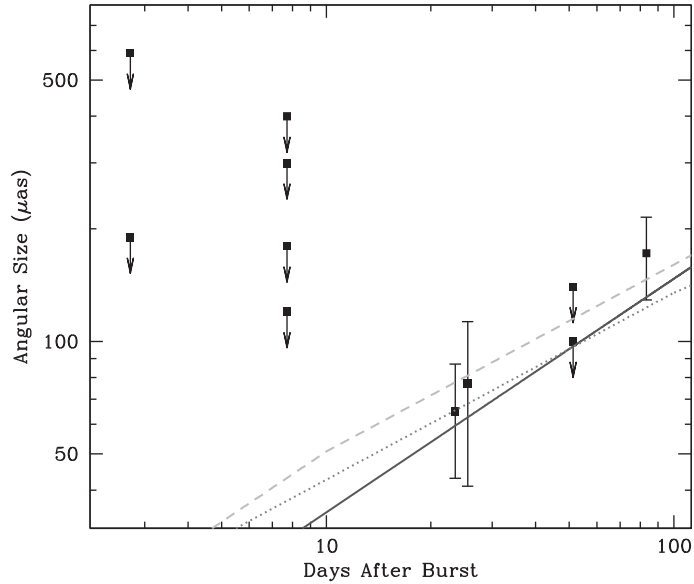
$$\frac{\tau_{\gamma\gamma}(\text{R})}{\tau_{\gamma\gamma}(\text{NR})} = \frac{f_{\text{R}} R_{\text{R}}^{-2}}{f_{\text{NR}} R_{\text{NR}}^{-2}} = \Gamma^{2\beta-2}. \quad (7.11)$$

For the typical value  $\beta \sim -2.2$ , this is a factor of  $\Gamma^{-6.4}$ . The pair production optical depth therefore drops significantly below unity if  $\Gamma$  is large enough. For the specific example discussed above,  $\Gamma > 220$  would solve the compactness problem if the original fraction factor is  $f \sim 0.2$ .

### 7.1.2 Superluminal Expansion of the Blastwave of GRB 030329

The relativistic motion of GRB ejecta was directly proven through observing the apparent size evolution of the afterglow region of the nearby GRB 030329 at  $z = 0.1685$ . Taylor et al. (2004) observed GRB 030329 using a Very Long Baseline Interferometry (VLBI) observational campaign with several large radio telescopes, and measured the apparent size of the radio source at different epochs. They found that the size of the afterglow is  $\sim 0.07$  mas (or 0.2 pc at the measured redshift) 25 days after the burst, and  $\sim 0.17$  mas (or 0.5 pc) 83 days after the burst. This led to an apparent expansion speed of  $3\text{--}5c$  (Fig. 7.1). Since apparent superluminal motion is possible only when an object moves with a relativistic speed and a small viewing angle (§3.2.3), this observation offers a definite proof for the relativistic motion of GRBs.

<sup>1</sup> This expression was first correctly derived by Lithwick and Sari (2001), after correcting some errors in many previous publications (e.g. Krolik and Pier, 1991; Fenimore et al., 1993; Woods and Loeb, 1995; Baring and Harding, 1997; Piran, 1999).

**Figure 7.1**

The apparent angular size of the radio afterglow source of GRB 030329 measured at different epochs which suggested superluminal expansion and, hence, relativistic motion of the source. The three lines are the expected evolution of the apparent angular size for different representations of the fireball model: solid: spherical fireball in a constant density medium; dotted: an early ( $t_j = 0.5$  days) jet model; dashed: a late ( $t_j = 10$  days) jet model. Reproduced from Figure 2 in Taylor et al. (2004) with permission. ©AAS.

### 7.1.3 Methods of Constraining $\Gamma$ from Observational Data

The bulk Lorentz factor  $\Gamma$  of a GRB is an important physical parameter. Unlike other parameters that can be directly measured (e.g. the isotropic energy  $E_{\gamma, \text{iso}}$  and luminosity  $L_{\gamma, \text{iso}}$ ),  $\Gamma$  is difficult to measure directly. One has to infer  $\Gamma$  through theoretical modeling. Below we introduce several methods for inferring  $\Gamma$ .

#### The Opacity Method

This method is closely related to the compactness problem argument discussed above. The logic is the following: high-energy photons are expected to be absorbed by low-energy photons to produce pairs if  $\Gamma$  is not large enough. The higher the photon energy, the lower the target photon energy and, hence, the larger the target photon number density  $n_{\text{ph}}$  (given the typical GRB Band-function spectra). As a result, higher energy photons give more stringent constraints on  $\Gamma$ . The detection of a photon with a certain energy then places a *lower limit* on  $\Gamma$ . The most stringent lower limit is obtained by the photon with the highest energy,  $\epsilon_{\gamma, \text{max}}$ . If photon attenuation due to pair production becomes significant beyond a particular energy, the high-energy spectrum may show a cutoff signature<sup>2</sup> beyond

<sup>2</sup> The cutoff is exponential for a steady jet. However, for an impulsive source, the time-integrated spectrum may show a power-law high-energy tail, which is progressively suppressed as the jet approaches a quasi-steady state (Granot et al., 2008).

a particular photon energy,  $\epsilon_{\gamma,\text{cut}}$ . If this cutoff energy is observed in the spectrum, one can assign  $\tau_{\gamma\gamma}(\epsilon_{\gamma,\text{cut}}) \sim 1$  and, hence, lead to a *measurement* of  $\Gamma$ .

Strictly speaking, this method can only constrain a certain combination of  $\Gamma$  and the unknown GRB emission site radius  $R_\gamma$  from the central engine. The pair production optical depth depends not only on  $\Gamma$ , but also sensitively on  $R_\gamma$ , i.e.  $\tau_{\gamma\gamma} \propto n_{\text{ph}} R_\gamma \propto R_\gamma^{-2}$ . One also needs to consider the curvature of the photon spectrum. It is possible that for the photon with energy  $\epsilon_{\gamma,\text{max}}$  or  $\epsilon_{\gamma,\text{cut}}$ , the target photon for producing pairs at the threshold,  $\epsilon_{\gamma,\text{th}}$ , may not belong to the same spectral segment as  $\epsilon_{\gamma,\text{max}}$  or  $\epsilon_{\gamma,\text{cut}}$ , so that the number density of the target photons has to be measured by fully taking into account the shape of the prompt emission spectrum.

A full derivation of  $\tau_{\gamma\gamma}(R, \Gamma)$  for three different spectral regimes of the target photons is presented in Gupta and Zhang (2008). Here we only write down the result of  $\tau_{\gamma\gamma}(R, \Gamma)$  in the most common regime, i.e. both  $\epsilon_{\gamma,\text{cut}}$  (or  $\epsilon_{\gamma,\text{max}}$ ) and  $\epsilon_{\gamma,\text{th}}$  are in the same spectral regime, the “ $\beta$ -portion” (spectral regime above  $E_p$ ) of the Band function.

We first re-write Eq. (7.8) in the form

$$\epsilon_{\gamma,\text{cut}}\epsilon_{\gamma,\text{th}} \sim \left( \frac{\Gamma}{1+z} \right)^2 (m_e c^2)^2, \quad (7.12)$$

where the redshift correction factor is included.

The following derivation follows Zhang and Pe’er (2009). Let us assume that the photon spectrum between  $\epsilon_{\gamma,\text{th}}$  and  $\epsilon_{\gamma,\text{cut}}$  can be well described as a power law

$$N(\epsilon_\gamma) = f_0 \epsilon_\gamma^\beta, \quad (7.13)$$

with  $\beta$  having a negative sign and a typical value  $\sim -2$ . Observationally, the coefficient  $f_0$  (in units of  $\text{ph cm}^{-2} (\text{keV})^{-1-\beta}$ ) can be directly fit from the data. If the spectrum is a Band function,  $f_0$  can be related to the Band-function parameters (Eq. (2.5)) through

$$f_0 = A \cdot \Delta T \left[ \frac{E_p(\alpha - \beta)}{(2 + \beta)} \right]^{\alpha - \beta} \exp(\beta - \alpha) (100 \text{ keV})^{-\beta}, \quad (7.14)$$

where  $\Delta T$  is the observed time interval during which the Band-function fit to the photon spectrum is performed.

Following the logic in §7.1.1 but performing a more rigorous integration, one can write the pair production optical depth in the form

$$\tau_{\gamma\gamma}(E_\gamma) = \frac{C(\beta)\sigma_T D_c^2(z)f_0}{-1 - \beta} \left( \frac{E_\gamma}{m_e^2 c^4} \right)^{-1-\beta} \frac{1}{R_\gamma^2} \left( \frac{\Gamma}{1+z} \right)^{2+2\beta}, \quad (7.15)$$

where  $D_c(z) = D_L(z)/(1+z)$  is the comoving distance to the GRB at redshift  $z$  (Eq. (2.41)), and  $C(\beta)$  is a function of  $\beta$  to reflect the averaging effect of pair production cross section in a wide energy range (Eq. (5.168)). Different authors have adopted different approximations:  $C(\beta) \simeq (7/6)(-\beta)^{-5/3}(1 - \beta)^{-1}$  for Svensson (1987),  $C(\beta) = (3/8)(1 - \beta)^{-1}$  for Gupta and Zhang (2008), and  $C(\beta) = 11/180$  for Lithwick and Sari (2001). For a typical value  $\beta = -2$ , the first two approximations agree with each other, while the last approximation is smaller by a factor of  $\sim 2$ .

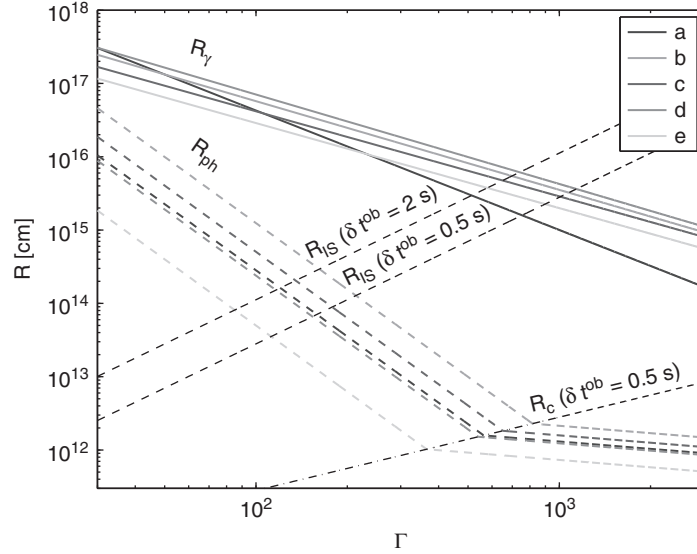


Figure 7.2

Constraints on  $\Gamma$  and  $R_\gamma$  (solid lines) based on the observational data of GRB 080916C (Abdo et al., 2009c). Different solid lines are derived using the highest photon energy  $\epsilon_{\gamma,\max}$  measured in different time intervals (a, b, c, d, and e) defined in Abdo et al. (2009c). Two parallel thin dashed lines denote the internal shock model with two assumed variability time scales. The thick dashed lines are the photosphere radius as a function of  $\Gamma$  for different time intervals. From Zhang and Pe'er (2009). A black and white version of this figure will appear in some formats. For the color version, please refer to the plate section.

This approach makes a direct connection between observations and the physical parameters  $\Gamma$  and  $R_\gamma$ . By solving  $\tau_{\gamma\gamma} = 1$  (making use of Eq. (7.15)) using the observationally determined parameters ( $A$ ,  $\alpha$ ,  $\beta$ ,  $E_p$ ,  $z$ , and most importantly  $\epsilon_{\gamma,\text{cut}}$  (or  $\epsilon_{\gamma,\max}$ )), one can define a line in  $\Gamma$ – $R_\gamma$  space that satisfies the compactness constraint. The GRB parameters should be on the line if  $\epsilon_{\gamma,\text{cut}}$  is measured, or should be above the line if  $\epsilon_{\gamma,\max}$  (a lower limit of  $\epsilon_{\gamma,\text{cut}}$ ) is measured. An example based on the observational data of GRB 080916C (Abdo et al. 2009c, see Fig. 2.9) is presented in Fig. 7.2 (Zhang and Pe'er, 2009).

Strictly speaking, this opacity method can only constrain the value or the range of  $\Gamma$  in the two-dimensional  $\Gamma$ – $R_\gamma$  plane. In order to constrain  $\Gamma$ , one needs to specify a relationship between  $R_\gamma$  and  $\Gamma$ . Most theoretical papers on this method (e.g. Baring and Harding, 1997; Lithwick and Sari, 2001) have adopted

$$R_\gamma = \Gamma^2 c \delta t / (1 + z), \quad (7.16)$$

where  $\delta t$  is the observed (minimum) variability time scale in the GRB lightcurves. By doing so, one has implicitly assumed an *internal shock* origin of the GRB emission. This relation defines another line in the  $\Gamma$ – $R_\gamma$  plane (black dashes in Fig. 7.2), which leads to a constraint on  $\Gamma$  (and  $R_\gamma$ ) at the intersection with the line defined by  $E_{\gamma,\text{cut}}$  or  $E_{\gamma,\max}$ . The *Fermi* team assumed Eq. (7.16) to constrain  $\Gamma$  for several bright GRBs detected by LAT, e.g. GRBs 080916C (Abdo et al., 2009c), 090510 (Ackermann et al., 2010), 090902B (Abdo et al., 2009b), 090926A (Ackermann et al., 2011), and 130427A (Ackermann et al., 2014).

While applying this method to constrain  $\Gamma$ , one should keep the following *caveats* in mind:

- The assumption of Eq. (7.16) is valid for the internal shock model. However, some other GRB prompt emission models may have a different  $R_\gamma$  from the one defined by Eq. (7.16). For example, the photosphere models of GRBs have  $R_\gamma \sim R_{\text{ph}}$  (Eqs. (7.65) and (7.68)), as discussed in §7.3.3 below, which is typically smaller than Eq. (7.16). Some magnetic reconnection and turbulence models (e.g. the ICMART model), on the other hand, interpret the minimum variability as the reconnection time scale of a reconnection unit (Zhang and Yan, 2011), and therefore have  $R_\gamma$  (much) greater than Eq. (7.16). Within these models, the inferred  $\Gamma$  can be larger or smaller than that inferred by assuming the validity of the internal shock model.
- The above treatment applies to a steady state. Since GRBs are impulsive events, photon opacity takes time to build up. Also high-energy  $\gamma$ -rays may be generated at a somewhat larger radius than the site of target MeV photons. These two effects reduce the optical depth, so that the inferred  $\Gamma$  can be smaller by a factor 2–3 than the inferred value without considering these two effects (Granot et al., 2008; Hascoët et al., 2012b).
- The above treatment applies to a “one zone” model. It is possible that GeV (high-energy) emission has an emission radius distinct from the target MeV emission. If so, the inferred  $\Gamma$  is further reduced (e.g. Zhao et al., 2011; Zou et al., 2011).

### The Afterglow Onset Method

Another commonly invoked method to constrain  $\Gamma$  is based on the *afterglow onset time*, or *deceleration time* of the relativistic blastwave. The idea is that the deceleration time  $t_{\text{dec}}$  for a constant density (ISM) medium is most sensitive to  $\Gamma$  but only weakly depends on other parameters, so that the Lorentz factor can be constrained from the measured  $t_{\text{dec}}$  and redshift (Eq. (7.81) below in §7.3.4). The optical afterglow lightcurve is predicted to rise before  $t_{\text{dec}}$  and decay after  $t_{\text{dec}}$  for both forward shock and (in most cases) reverse shock emission components (see details in Chapter 8). As a result,  $t_{\text{dec}}$  can be measured as the peak time in the early optical afterglow lightcurve. Compared to the opacity method, this method has fewer uncertainties. Nonetheless the following *caveats* should be kept in mind:

- The measured  $\Gamma$  is the Lorentz factor at the deceleration radius. It can be somewhat different from the Lorentz factor during the prompt emission phase. Since a significant fraction of GRB outflow energy is released in the form of radiation energy during the prompt emission phase,  $\Gamma$  during the prompt emission phase may be higher than  $\Gamma$  at the deceleration time for matter-dominated models (say, by a factor of 2). If the outflow is Poynting flux dominated, the outflow may be still in the *acceleration* phase during prompt emission (see §7.5 below). The relation between the  $\Gamma$  values measured in the two epochs (prompt emission and early afterglow) is more complicated. In any case, a discrepancy of a factor of 1–2 between the  $\Gamma$  values inferred using the two methods is allowed.
- The expression of  $t_{\text{dec}}$  depends on the density profile of the ambient medium (§7.3 below), and whether there is additional energy injection during the deceleration phase.



For more complicated deceleration models, the dependence of  $t_{\text{dec}}$  on other parameters is no longer weak, so that the inferred  $\Gamma$  would have a larger uncertainty than the simplest case assuming a constant energy and constant ambient medium density.

- Not all GRBs have an early afterglow lightcurve bump detected. For some GRBs, the optical lightcurve is decaying from the first detected data point. For these cases, only a *lower limit* of  $\Gamma$  can be derived.

## Photosphere Method

Within the framework of the matter-dominated “fireball” scenario, Pe’er et al. (2007) showed that the photosphere emission carries the information about the *energy-to-mass ratio*  $\eta$  of the fireball if  $\eta$  does not exceed a critical value  $\eta_*$  (see §7.3.3 below). In this regime ( $\eta < \eta_*$ ), the bulk Lorentz factor  $\Gamma$  in the coasting regime is simply  $\eta$ , which can be estimated from the temperature and flux of the photosphere emission. The details of this method will be discussed later in §7.3.3 and §9.3. The *caveats* of this method include the following:

- If  $\eta > \eta_*$  is satisfied the photosphere properties do not depend on  $\Gamma$ , so  $\Gamma$  cannot be inferred.
- If the GRB outflow is not a pure fireball, then the photosphere temperature and flux depend not only on  $\eta$ , but also on  $\sigma_0$  at the central engine. A generalized treatment was presented by Gao and Zhang (2015), who showed that both  $\eta$  and  $\sigma_0$  may be inferred from the data if one assumes the value of the inner radius of the central engine  $R_0$ . This will be discussed in detail in §9.3.

## Other Methods

Several other methods to estimate  $\Gamma$  have been discussed in the literature.

- Zou and Piran (2010) proposed that, by investigating the quiescent period of GRB prompt emission, one may set an *upper limit* on  $\Gamma$ . This is because the external shock is supposed to grow during the prompt emission phase. If  $\Gamma$  is large enough, a smooth, underlying external shock component may already have significant flux during the prompt emission phase and may be observable during the quiescent period. A non-detection of this flux would place an upper limit on  $\Gamma$ . In practice this method can be applied only to a limited number of GRBs.
- If the steep decay segment of GRB prompt emission or X-ray flare is due to the curvature effect (§3.4.4), the observed duration of the tail emission may be related to the emission radius  $R_\gamma$  and the jet opening angle  $\theta_j$  through (Zhang et al., 2006)

$$t_{\text{tail}} \leq (1+z) \frac{R_\gamma}{c} (1 - \cos \theta_j) \simeq (1+z) \frac{R_\gamma}{c} \frac{\theta_j^2}{2}. \quad (7.17)$$

The  $\leq$  sign takes into account the possibility that the true tail duration may be longer than what is observed, since often another emission component emerges before the decay segment completely dies out. If the emission radius  $R_\gamma$  can be related to the bulk Lorentz

factor  $\Gamma$  (e.g. in the internal shock model), one can use  $t_{\text{tail}}$  and other information to constrain the lower limit of  $\Gamma$  (Jin et al., 2010; Yi et al., 2015). This method has been applied to X-ray flares to constrain their bulk Lorentz factors.

- Zou et al. (2015) suggested that for the GRBs that show a photospheric-origin thermal component, in view that the observed variability time scale should satisfy  $\delta t \geq (1 + z)R_{\text{ph}}/2\Gamma^2c$ , a simple lower limit of  $\Gamma$  can be obtained using the observed thermal flux and temperature for a GRB with known redshift  $z$ , i.e.

$$\Gamma \geq \left[ \frac{F_{\text{thermal}}^{\text{obs}} D_L^2}{(1+z)^2 \sigma_B T_{\text{obs}}^4 (2c\delta t)^2} \right]^{1/2}, \quad (7.18)$$

where  $\sigma_B$  is the Stefan–Boltzmann constant.

## Results

Although with large uncertainties, the Lorentz factors  $\Gamma$  of a good sample of GRBs have been estimated (Fig. 7.3, see Racusin et al. 2011 and references therein; Exercise 7.1).

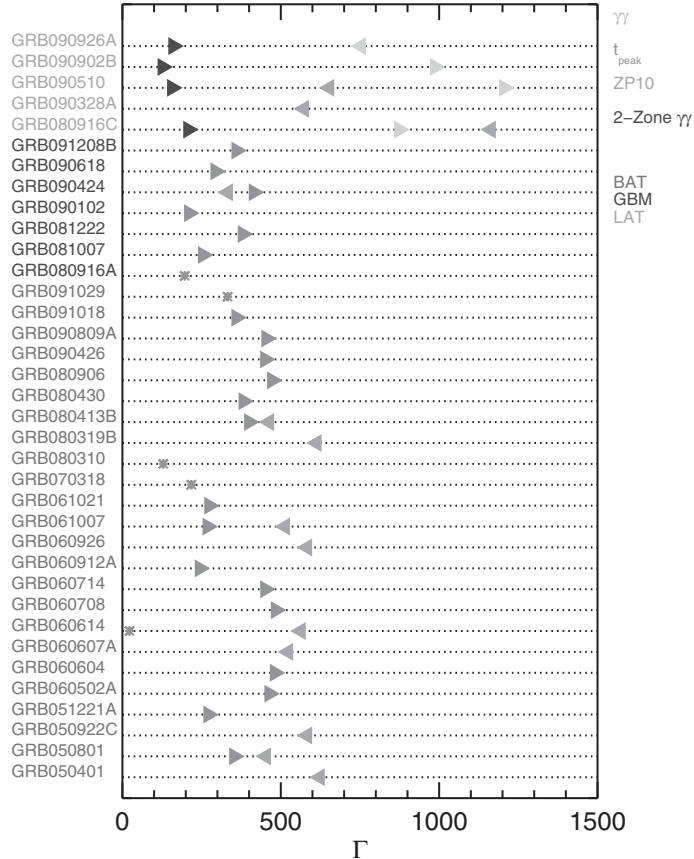


Figure 7.3

The constrained Lorentz factors of GRBs using various methods. From Racusin et al. (2011). A black and white version of this figure will appear in some formats. For the color version, please refer to the plate section.

Typically, the constrained  $\Gamma$  values are above 100 and below 1000. The LAT GRBs are found to have  $\Gamma$  close to or exceeding 1000 (e.g. Abdo et al., 2009c,b; Ackermann et al., 2010, 2011) based on the opacity method and the internal shock model. However, as discussed above, this method has some uncertainties, and may have overestimated  $\Gamma$  (e.g. the emission radius of GeV emission may be larger than  $\Gamma^2 c \delta t$ ).

The bulk Lorentz factors of X-ray flares have also been constrained using some of the above-mentioned methods. The typical lower limit is a few tens (Jin et al., 2010; Yi et al., 2015). Even though their Lorentz factors are somewhat lower than those of GRBs, X-ray flares are still highly relativistic events.

## 7.2 A General Theoretical Framework

After establishing the relativistic nature of the GRB outflow, we now discuss a general theoretical framework of GRBs.

### 7.2.1 Key Ingredients of the Models

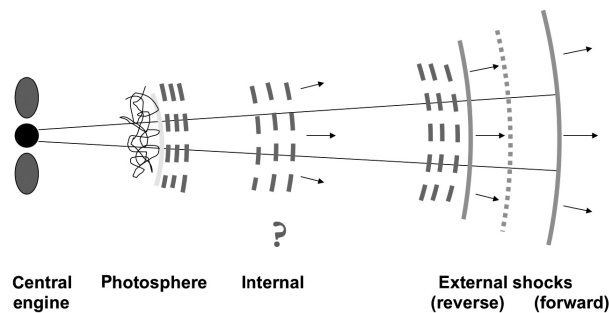
Many different theoretical models for GRBs have been discussed in the literature, especially for interpreting the prompt emission. Most of these models share some of the key ingredients listed below.

- A progenitor star undergoes a catastrophic event, resulting in a sudden release of gravitational energy.
- After the catastrophic event, a central engine is formed. This central engine continuously powers an *outflow* for a certain duration of time, during which *gravitational energy* (for accreting systems) or *spin energy* (for spindown systems) is released in the form of *thermal energy* or *Poynting flux energy*, respectively.
- The outflow is likely *collimated* into a relativistic jet during propagation.
- The thermal energy and/or Poynting flux energy are partially converted to *kinetic energy* of the outflow, making the ejecta reach a relativistic speed.
- A fraction of the initial thermal energy is released in the form of photons at the *photosphere* of the outflow.
- The remaining kinetic energy and/or Poynting flux energy are “dissipated” *internally* within the jet and get converted to (random) *internal energy* of particles in *internal shocks* (for kinetic energy) or *magnetic dissipation sites* (for Poynting flux energy).
- A fraction of internal energy is given to leptons (electrons and sometimes  $e^+e^-$  pairs) and gets radiated almost completely as *electromagnetic radiation* to power the non-thermal GRB *prompt emission*.
- After the prompt emission phase, the jet is decelerated by a *circumburst ambient medium*, as a relativistic forward shock propagates into the medium. Early on, a reverse shock propagates into the jet itself and crosses the jet in a short duration of time. If the central engine is long lived or if the ejecta has a Lorentz factor “stratification” (a wide

distribution of  $\Gamma$ ), the reverse shock can be long lived. Emission from these *external shocks* powers the long-lasting *afterglow* emission of GRBs.

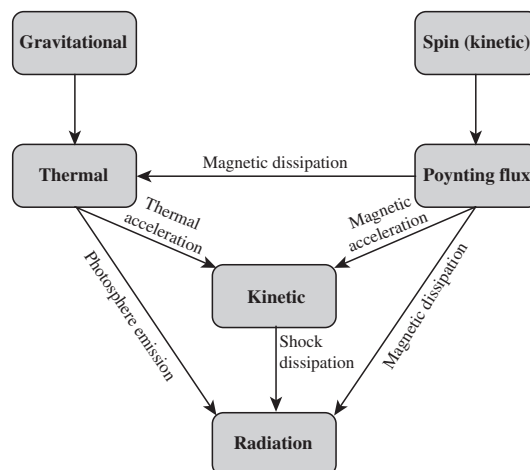
- The spatial range between the photosphere (included) and the external forward/reverse shocks (excluded) is called the *internal* emission site of a GRB. GRB prompt emission likely originates from one or more internal emission regions. The radiation mechanism of prompt emission is an open question. The leading candidates include *synchrotron radiation* from an optically thin region, and a *quasi-thermal, Comptonized* emission near the photosphere. *Synchrotron self-Compton* (SSC), *external inverse Compton* (EIC), and *hadronic cascade* have also been discussed in the literature to account for (part of) the prompt emission spectra.
- The main radiation mechanism of afterglow emission has been identified as *synchrotron radiation* from the external shocks.

Figure 7.4 is a cartoon picture of the evolution of a GRB jet within this general theoretical framework. Figure 7.5 outlines the energy flow in a GRB jet, describing how various forms of energy convert from one to another and give rise to the observed radiation from GRBs.



**Figure 7.4**

A cartoon picture of the evolution of a GRB jet within the general theoretical framework of GRBs. The dashed curves denote possible internal emission sites, which are bracketed by the photosphere (included) and the external shocks (excluded).



**Figure 7.5**

An energy flow chart for GRBs.

### 7.2.2 A Brief Quantitative Description

Within the above-mentioned general theoretical framework, the dynamical evolution of the jet is determined by the *initial conditions* at the central engine.

For a *fireball* (magnetic fields negligible), the key central engine parameters include the time-dependent *matter luminosity*  $L_{m,0}(t)$  (to be differentiated from the *Poynting flux luminosity*  $L_{P,0}(t)$  introduced below), baryon loading rate  $\dot{M}(t)$ , and the *energy per baryon*

$$\eta(t) \equiv \frac{L_{m,0}(t)}{\dot{M}(t)c^2}. \quad (7.19)$$

Averaging over a duration  $\Delta t$  (say within a broad pulse of a GRB or the entire duration of the GRB), one can define a mean energy-to-mass ratio

$$\eta \equiv \frac{Mc^2 + E_{th,0}}{Mc^2} = 1 + \frac{U_{th,0}}{nm_p c^2}, \quad (7.20)$$

where  $E_{th,0}$  is the initial fireball thermal energy at the central engine,  $U_{th,0}$  is the initial thermal energy density,  $M$  is the total mass loading in the fireball, and  $n$  is the baryon particle number density, and hydrogen gas is considered for simplicity.

If the central engine also carries a strong magnetic field, one can define a *generalized magnetization parameter*  $\sigma_0$ , which is the ratio of the initial Poynting flux luminosity  $L_{P,0}(t)$  and the initial matter flux  $L_{m,0}(t) = \eta\dot{M}(t)c^2$  (which includes the thermal energy as well). So the magnetization parameter

$$\sigma_0(t) \equiv \frac{L_{P,0}(t)}{\eta(t)\dot{M}(t)c^2}, \quad (7.21)$$

or on average

$$\sigma_0 \equiv \frac{L_{P,0}}{\eta\dot{M}c^2} = \frac{E_{P,0}}{\eta Mc^2} = \frac{B_0^2}{4\pi\eta\rho_0 c^2}, \quad (7.22)$$

where  $L_{P,0}$  is the average Poynting luminosity  $\propto |\mathbf{E} \times \mathbf{B}|/(4\pi)$  (with  $E \simeq B$ ),  $E_{P,0}$  is the total initial Poynting flux energy launched within  $\Delta t$ , and  $\dot{M}$  is the average mass loading rate during  $\Delta t$ . In the last equation, the Poynting flux energy density  $B_0^2/4\pi$  and matter energy density (including thermal energy, assuming no bulk motion)  $\eta\rho_0 c^2$  at the central engine have been used. For a “cold” central engine (no fireball component), one has  $\eta \sim 1$  and  $\sigma_0 \gg 1$ .

Including both the *hot (fireball)* and *cold (Poynting flux)* components, the central engine can be defined by the parameter

$$\mu_0(t) = \frac{L_{w,0}(t)}{\dot{M}(t)c^2} = \frac{L_{m,0}(t) + L_{P,0}(t)}{\dot{M}(t)c^2} = \eta(t)[1 + \sigma_0(t)], \quad (7.23)$$

or on average

$$\mu_0 = \frac{E_{tot,0}}{Mc^2} = \frac{Mc^2 + E_{th,0} + E_{P,0}}{Mc^2} = \eta(1 + \sigma_0). \quad (7.24)$$

Here  $L_{w,0}(t)$  is the initial luminosity of the central engine “wind”, and  $E_{tot,0}$  is the initial total energy of the ejecta (including both matter energy and Poynting flux energy).

The ejecta undergo complicated evolution after leaving the central engine. At various sites (photosphere and other energy dissipation sites), photons escape so that the total energy of the system decreases with time. Besides this energy loss, the rest of the energy is conserved, and is converted from one form to another (Fig. 7.5). During the early acceleration phase, the thermal energy and Poynting flux energy (partially) are converted to the kinetic energy of the outflow. For a slice of wind ejected at a particular engine time, at any radius<sup>3</sup>  $r$  one may define

$$\mu(r) = \frac{E_{\text{tot}}(r)}{Mc^2} = \Gamma(r)\Theta(r)(1 + \sigma(r)), \quad (7.25)$$

where  $\Gamma(r)$  is the bulk Lorentz factor,  $\Theta(r)$  is the total comoving energy per baryon ( $\Theta - 1$  is the internal energy), and

$$\sigma(r) = \frac{L_p(r)}{L_m(r)} = \frac{B(r)^2}{4\pi\Gamma(r)\Theta(r)\rho(r)c^2} = \frac{B'(r)^2}{4\pi\Theta(r)\rho'(r)c^2} \quad (7.26)$$

is the generalized magnetization parameter, all at the radius  $r$ ;  $B$ ,  $B'$  are the magnetic field strengths in the lab frame and comoving frame, respectively;  $\rho$  and  $\rho'$  are the mass density of the ejecta in the lab frame and comoving frame, respectively; and  $L_p(r)$  and  $L_m(r)$  are the Poynting flux and matter flux (kinetic plus rest energy flux) at  $r$ , respectively.

Neglecting radiative energy loss, one has  $\mu = \mu_0$ , or

$$\mu_0 = \eta(1 + \sigma_0) = \Gamma\Theta(1 + \sigma). \quad (7.27)$$

Magnetic acceleration ensures that  $\sigma$  drops with time, so that  $\Gamma$  increases with time. Ultimately, the flow would achieve the asymptotic maximum Lorentz factor

$$\Gamma_{\text{max}} = \mu_0 \simeq \begin{cases} \eta, & \sigma_0 \ll 1, \\ 1 + \sigma_0, & \eta \sim 1. \end{cases} \quad (7.28)$$

In reality, the outflow is decelerated at the *deceleration radius*  $R_{\text{dec}}$ . If the ejecta can reach  $\Gamma_{\text{max}}$  at a *coasting radius*  $R_c < R_{\text{dec}}$ , then the maximum Lorentz factor is achievable. Conversely, if  $R_c$  satisfies  $R_c > R_{\text{dec}}$ , then before  $\Gamma_{\text{max}}$  is achieved the outflow already undergoes deceleration. This may happen when  $\sigma_0 \gg 0$ , since magnetic acceleration is relatively slow (see §7.4 and §7.5 below). For fireballs (§7.3),  $R_c$  is always smaller than  $R_{\text{dec}}$  for typical parameters of GRBs, so that  $\Gamma_{\text{max}}$  can reach  $\eta$  if  $\eta$  does not exceed a critical value  $\eta_*$  (see §7.3.3 and Eq. (7.71) below).

## 7.3 Fireball

A *fireball* corresponds to the  $\sigma_0 \ll 1$  regime. Since the Poynting flux term is neglected, the system can be treated with relativistic hydrodynamics, which is much simpler than relativistic MHD.

<sup>3</sup> Throughout the book, the lower case letter  $r$  is adopted to denote a *variable* radius, while the upper case letter  $R$  is adopted to denote various characteristic radii with specific physical meaning, such as  $R_c$ ,  $R_{\text{ph}}$ ,  $R_{\text{dec}}$ , etc.

### 7.3.1 Dynamical Evolution of the Fireball

The dynamical evolution of a fireball includes three phases: *acceleration*, *coasting*, and *deceleration*.

#### Fireball Acceleration

The acceleration phase was studied in detail by Mészáros et al. (1993), Piran et al. (1993), and Kobayashi et al. (1999). The basic scaling is initially  $\Gamma \propto r$ , i.e. the Lorentz factor increases linearly with the radius  $r$ , and later  $\Gamma \sim \text{const}$  after most of the thermal energy is converted to kinetic energy. We derive this scaling analytically below, following Piran et al. (1993).

We start with the relativistic energy–momentum tensor

$$T^{\mu\nu} = \mu u^\mu u^\nu + p g^{\mu\nu}, \quad (7.29)$$

where  $u^\mu$  is the 4-velocity,  $g^{\mu\nu}$  is the metric, and

$$\mu = nm_p c^2 + e + p = nm_p c^2 + \frac{\hat{\gamma}}{\hat{\gamma} - 1} p \quad (7.30)$$

is specific enthalpy density,  $\hat{\gamma}$  is adiabatic index ( $p \propto n^{\hat{\gamma}}$ ), which is  $\sim 4/3$  for a relativistic gas,  $e$  is internal energy density, and  $p = (\hat{\gamma} - 1)e$  is pressure.

Let us consider the free expansion of an isotropic fireball. The three (mass, energy, momentum) conservation equations (Eqs. (4.9), (4.11), and (4.10)) can be reduced to a simple form with one spatial dimension ( $r$  coordinate) only (Exercise 7.2). It is more convenient to adopt  $m_p = 1$  and  $c = 1$  to simplify the equations, so that the three equations can be cast in the form:

$$\frac{\partial}{\partial t}(n\Gamma) + \frac{1}{r^2} \frac{\partial}{\partial r}(r^2 n u) = 0, \quad (7.31)$$

$$\frac{\partial}{\partial t}(e^{3/4} \Gamma) + \frac{1}{r^2} \frac{\partial}{\partial r}(r^2 e^{3/4} u) = 0, \quad (7.32)$$

$$\frac{\partial}{\partial t} \left[ \left( n + \frac{4}{3} e \right) \Gamma u \right] + \frac{1}{r^2} \frac{\partial}{\partial r} \left[ r^2 \left( n + \frac{4}{3} e \right) u^2 \right] = -\frac{1}{3} \frac{\partial e}{\partial r}, \quad (7.33)$$

where  $u = \Gamma \beta = \sqrt{\Gamma^2 - 1}$  is the 4-speed.

One may change variables from  $(r, t)$  to  $(r, s = t - r)$ . The equations then become ( $\hat{\gamma} = 4/3$  adopted)

$$\frac{1}{r^2} \frac{\partial}{\partial r}(r^2 n u) = -\frac{\partial}{\partial s} \left( \frac{n}{\Gamma + u} \right), \quad (7.34)$$

$$\frac{1}{r^2} \frac{\partial}{\partial r}(r^2 e^{3/4} u) = -\frac{\partial}{\partial s} \left( \frac{e^{3/4}}{\Gamma + u} \right), \quad (7.35)$$

$$\frac{1}{r^2} \frac{\partial}{\partial r} \left( r^2 \left( n + \frac{4}{3} e \right) u^2 \right) = -\frac{\partial}{\partial s} \left[ \left( n + \frac{4}{3} e \right) \frac{u}{\Gamma + u} \right] + \frac{1}{3} \left[ \frac{\partial e}{\partial s} - \frac{\partial e}{\partial r} \right]. \quad (7.36)$$

Within this notation, the derivative  $\partial/\partial r$  refers to constant  $s = t - r$ , i.e. is calculated along a characteristic outwards motion with speed of light. Piran et al. (1993) argued that, for a relativistic fireball ( $\Gamma \gg 1$ ), the right hand side of all three equations is very small, so they take them as  $\sim 0$ . Taking  $u \simeq \Gamma$  for this regime, Eqs. (7.34)–(7.36) are reduced to

$$r^2 n \Gamma \sim \text{const}, \quad (7.37)$$

$$r^2 e^{3/4} \Gamma \sim \text{const}, \quad (7.38)$$

$$r^2 \left( n + \frac{4}{3} e \right) \Gamma^2 \sim \text{const}. \quad (7.39)$$

In the radiation-dominated phase (early acceleration phase), one has  $e \propto T^4 \gg n$ ; one therefore has

$$\Gamma \propto r, \quad n \propto r^{-3}, \quad e \propto r^{-4}, \quad T_{\text{obs}} \simeq \Gamma T \sim \text{const}. \quad (7.40)$$

Alternatively, in the matter-dominated phase (late coasting phase), one has  $e \ll n$ , so that

$$\Gamma \sim \text{const}, \quad n \propto r^{-2}, \quad e \propto r^{-8/3}, \quad T_{\text{obs}} \simeq \Gamma T \propto r^{-2/3}. \quad (7.41)$$

### Coasting and Deceleration

After the fireball reaches the maximum Lorentz factor, it moves with a constant Lorentz factor. This is the *coasting* phase. Internal shocks may develop during this phase, which would globally reduce the average Lorentz factor of the outflow (with the expense of releasing energy in the form of photons and neutrinos). The fireball is eventually decelerated by the circumburst medium (see §7.3.4 and Chapter 8 for details).

A schematic graph that shows the global  $\Gamma$  evolution for a fireball is presented in the upper panel of Fig. 7.6.

The dynamical evolution of a fireball was studied numerically by Mészáros et al. (1993) and Kobayashi et al. (1999). Lower panels in Fig. 7.6 display the numerical results of Kobayashi et al. (1999), which are generally consistent with the analytical estimates (except that they did not model internal shocks).

#### 7.3.2 Characteristic Radii

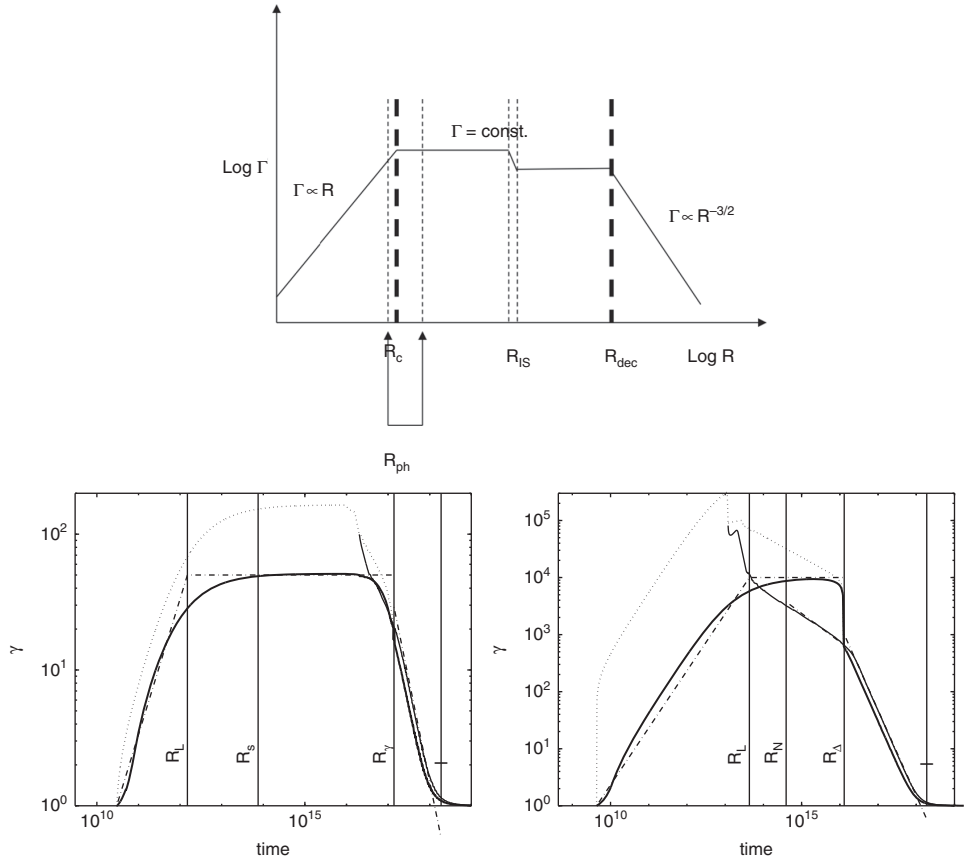
For a fireball expanding into a circumburst medium, there are several characteristic radii, which we outline below. Two important radii, the photosphere radius,  $R_{\text{ph}}$ , and the deceleration radius,  $R_{\text{dec}}$ , are discussed separately in §7.3.3 and §7.3.4.

#### Base of Fireball: $R_0$

This is the radius where the fireball is launched.

For a “naked” central engine (i.e. the engine is not buried inside the progenitor star),  $R_0$  is essentially the size of the central engine system itself. For a hyper-accreting black hole,  $R_0$  may be taken as the innermost radius of the accretion disk, i.e.  $R_0 \sim 3r_g = 6GM/c^2 = 9 \times 10^6 \text{ cm}(M/10M_\odot)$  for a Schwarzschild black hole, or  $R_0 \sim r_g = 2GM/c^2 = 3 \times 10^6 \text{ cm}(M/10M_\odot)$  for a prograding Kerr black hole. For a millisecond magnetar, the base



**Figure 7.6**

The dynamical evolution of a fireball. *Upper panel:* A cartoon picture of the average  $\Gamma$  evolution of a fireball. *Lower panels:* Numerical results of  $\Gamma$  evolution of a fireball for the thin shell (left) and thick shell (right) cases. Reproduced from Figure 2 in Kobayashi et al. (1999) with permission. ©AAS.

may be taken as the radius of the light cylinder  $R_0 \sim R_{LC} = c/\Omega = cP/2\pi \sim 5 \times 10^6 \text{ cm} P_{-3}$ , where  $P_{-3} = P/10^{-3} \text{ s}$ . Both types of central engines have  $R_0$  of the same order. One may take

$$R_0 = (10^7 \text{ cm}) R_{0,7} \quad (7.42)$$

for a naked engine, without specifying the nature of the engine.

For a long-duration GRB whose progenitor is likely a massive star, the jet initially needs to penetrate through the heavy stellar envelope. The engine is therefore not “naked”, at least during the early phase. A fireball can be “re-born” after the jet emerges from the star. So, effectively, one may take the outer boundary of the star as the base of the fireball. Since the progenitor of a GRB usually gives rise to a Type Ic supernova, the progenitor star should have its H and most He envelopes stripped. The size of such a Wolf–Rayet progenitor star is  $R_* \sim 10^{11} \text{ cm}$ . The size of the central engine may be adopted as the cross section of the jet at the surface of the star, i.e.

$$R_0 \sim R_* \theta_j = (10^{10} \text{ cm}) R_{*,11} \theta_{j,-1}. \quad (7.43)$$

Let us parameterize  $L_w$  as the initial luminosity of the GRB fireball wind. At the central engine  $R_0$ , the energy is mostly in the thermal form. The initial temperature of the fireball  $T_0$  depends on  $L_w$  and  $R_0$ , which can be estimated as

$$T_0 \simeq \left( \frac{L_w}{4\pi R_0^2 g_0 \sigma_B} \right)^{1/4} \simeq (1.5 \times 10^{10} \text{ K}) L_{w,52}^{1/4} R_{0,7}^{-1/2}, \quad (7.44)$$

$$kT_0 \simeq (1.3 \text{ MeV}) L_{w,52}^{1/4} R_{0,7}^{-1/2}, \quad (7.45)$$

$$\Theta_0 \equiv \frac{kT_0}{m_e c^2} \simeq 2.5 L_{w,52}^{1/4} R_{0,7}^{-1/2}. \quad (7.46)$$

Here  $\sigma_B = (\pi^2 k^4)/(60c^2 \hbar^3) \simeq 5.67 \times 10^{-5} \text{ erg cm}^{-2} \text{ s}^{-1} \text{ K}^{-4}$  is the Stefan–Boltzmann constant, and isotropic emission is assumed.

The effective degree of freedom parameter  $g_0 = 2.75$  has been adopted for GRB fireballs. This can be derived as follows (Kumar and Zhang, 2015). The total number of massless degrees of freedom is written as (Eq. (3.62) of Kolb and Turner 1990)

$$g_* = \sum_{i=\text{bosons}} g_i \left( \frac{T_i}{T} \right)^4 + \frac{7}{8} \sum_{i=\text{fermions}} g_i \left( \frac{T_i}{T} \right)^4. \quad (7.47)$$

At the base of the fireball (central engine) the photons are in equilibrium with  $e^\pm$  pairs and a small amount of baryons (protons and possibly neutrons as well). Since  $kT_0 > m_e c^2$  but  $\ll m_p c^2$ , only leptons can be regarded as “massless” and therefore contribute to the degrees of freedom. Since each photon, electron, and positron has two spin states, the total degree of freedom is then  $2 + (7/8) \times 2 \times 2 = 5.5$ . The internal energy of a gas with a mix of bosons and fermions with a total number of massless degrees of freedom can be written (Eq. (3.61) of Kolb and Turner 1990, but with factor  $k^4/(c\hbar)^3$  explicitly included)

$$u = \frac{\pi^2}{30} g_* \frac{k^4}{c^3 \hbar^3} T^4 = \frac{g_*}{2} a T^4 = g_0 a T^4, \quad (7.48)$$

where  $a = 4\sigma_B/c = (\pi^2/15)(k^4/c^3 \hbar^3) \simeq 7.56 \times 10^{-15} \text{ erg cm}^{-3} \text{ K}^{-4}$  is the Stefan–Boltzmann energy density constant (Eq. (1.58b) of Rybicki and Lightman 1979). One can see that the effective degree of freedom is

$$g_0 = g_*/2 = [2 + (7/8) \times 2 \times 2]/2 = 2.75. \quad (7.49)$$

For an isotropic source, the outgoing flux  $F = L_w/4\pi R_0^2$  from the base of the fireball is  $F = cu/4$ ; one can then derive Eq. (7.44), noting  $\sigma_B = ac/4$ . It is worth noting that, in the literature, sometimes  $g_0 \sigma_B$  is replaced by  $ac$  (e.g. Mészáros and Rees, 2000b; Gao and Zhang, 2015). The estimated central engine temperature is then smaller by a factor  $(4/2.75)^{1/4} \simeq 1.1$ .

## Shell Width

For a continuous wind lasting for duration  $\Delta t$ , a shell with finite width is ejected from the central engine. This width enters the definitions of some characteristic radii, so we dedicate a space to it. Most of the discussion below in the rest of §7.3.2 follows Piran (1999).

**Table 7.1** Evolution of the shell width in the comoving and lab frames

Radius regime	$\Delta'$	$\Delta$
$\Delta_0 < r < R_c$	$r$	$\Delta_0$
$R_c < r < R_s$	$R_c$	$\Delta_0$
$R_s < r < R_{\text{dec}}$	$r/\Gamma_0$	$r/\Gamma_0^2$
$r > R_{\text{dec}}$	$r/\Gamma$	$r/\Gamma^2$

Since the shell quickly attains a relativistic speed, one may estimate the initial width of the shell as

$$\Delta_0 \sim c\Delta t = (3 \times 10^7 \text{ cm})\Delta t_{-3}. \quad (7.50)$$

During the expansion, the comoving width  $\Delta' \sim \Gamma \Delta_0$  increases with time. The lab-frame width (also the width seen by a  $90^\circ$  observer)  $\Delta \sim \Delta'/\Gamma \sim \Delta_0$  remains unchanged. This width remains  $\Delta_0$  until reaching the spreading radius  $R_s$  (discussed below), above which sound waves propagate across the shell, and the lab-frame shell width starts to increase with radius as  $\Delta \sim R/\Gamma^2$ . The comoving width changes as  $\Delta' \sim R/\Gamma$ . Overall, the evolution of the shell width is summarized in Table 7.1.

### Coasting Radius: $R_c$

During the acceleration phase, one has  $\Gamma \propto r$ . The fireball “coasts” after reaching the maximum Lorentz factor  $\Gamma_0$ .<sup>4</sup>

For a short-duration shell with  $\Delta_0 < R_0$ , the coasting radius is

$$R_c \simeq R_0 \Gamma_0 \simeq (10^9 \text{ cm}) \Gamma_2 R_{0.7}. \quad (7.51)$$

For a long-duration shell with  $\Delta_0 \gg R_0$ , the front of the shell reaches maximum Lorentz factor  $\Gamma_0$  around the radius defined by (7.51). However, the entire shell reaches the maximum Lorentz factor (and therefore coasts) at a larger radius defined by

$$R_c \simeq \Delta_0 \Gamma_0 = (10^{10} \text{ cm}) \Gamma_2 \Delta_{0.8}. \quad (7.52)$$

### Spreading Radius: $R_s$

The sound speed of a relativistic gas ( $\hat{\gamma} = 4/3$ ) is (Eq. (4.55))

$$c_s \equiv \left( \frac{\partial p}{\partial \rho} \right)^{1/2} \simeq \frac{c}{\sqrt{3}} \simeq 0.58c. \quad (7.53)$$

<sup>4</sup> Neglecting energy dissipation in internal shocks, the maximum Lorentz factor during the coasting phase is also the initial Lorentz factor of the ejecta during the deceleration (afterglow) phase. Here we use the same symbol  $\Gamma_0$  to denote this Lorentz factor.

If a sound wave has time to propagate across a shell, the shell will spread globally. In the comoving frame, the shell width may be estimated as

$$\Delta' = \Delta'_0 + c_s t' = \Delta'_0 + c_s \frac{t}{\Gamma_0}, \quad (7.54)$$

and in the lab frame the width is

$$\Delta = \frac{\Delta'}{\Gamma_0} = \frac{\Delta'_0}{\Gamma_0} + c_s \frac{t'}{\Gamma_0} = \Delta_0 + c_s \frac{t}{\Gamma_0^2}. \quad (7.55)$$

Here  $t'$  and  $t$  are the shell propagation times in the comoving and lab frames, respectively.

When the second term is larger than the first term, i.e.  $t > t_s = \Gamma_0^2 \Delta_0 / c_s$ , the shell width starts to spread significantly. This occurs at the spreading radius

$$R_s = \beta c t_s = \frac{\beta c}{c_s} \Gamma_0^2 \Delta_0 \simeq 1.7 \Gamma_0^2 \Delta_0 \sim \Gamma_0^2 \Delta_0. \quad (7.56)$$

In the spreading phase, one has (Table 7.1)

$$\Delta \sim \frac{r}{\Gamma_0^2}, \quad \Delta' \sim \frac{r}{\Gamma_0}. \quad (7.57)$$

### Internal Shock Radius: $R_{\text{IS}}$

For a violent, erratic source such as a GRB, it is natural to expect internal non-uniformity within the wind launched by the central engine. Let us suppose that two mini-shells are ejected with a separation time of  $\Delta t$  and with different Lorentz factors: i.e. a slower shell with  $\Gamma_s$  is leading a faster one with  $\Gamma_f$ . According to §3.5.2, a pair of internal shocks occur at the catch-up radius, which reads

$$R_{\text{IS}} \simeq 2\Gamma_s^2 c \Delta t. \quad (7.58)$$

This is the site of non-thermal  $\gamma$ -ray emission within the framework of the fireball shock model (Rees and Mészáros, 1994; Daigne and Mochkovitch, 1998).

### 7.3.3 Photosphere

The *photosphere radius*  $R_{\text{ph}}$  is defined as the radius above which the photon optical depth for Thomson scattering is below unity, i.e.

$$\int_{R_{\text{ph}}}^{\infty} d\tau = \int_{R_{\text{ph}}}^{\infty} n_e \sigma_T ds = 1, \quad (7.59)$$

where

$$n_e = \frac{L_w \mathcal{Y}}{4\pi r^2 c \eta m_p c^2} \quad (7.60)$$

is the electron number density in the lab frame (which is also the electron number density seen by a  $90^\circ$  observer), and  $\mathcal{Y}$  denotes the pair multiplicity parameter.<sup>5</sup> The spatial

<sup>5</sup> For a more general jet composition with a non-negligible magnetization parameter  $\sigma$ , the  $L_w$  term should be replaced by  $L_w/(1 + \sigma)$ . See §9.3.3 for a treatment.

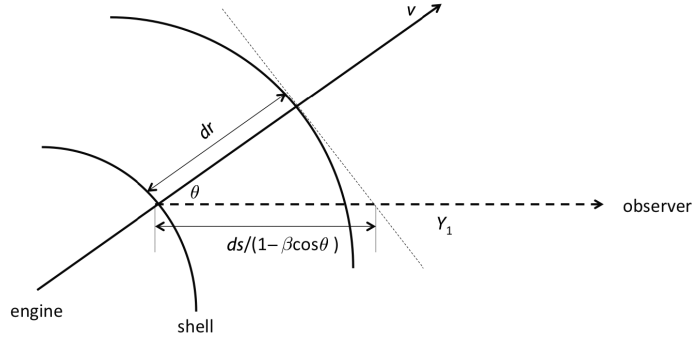


**Figure 7.7** The geometry for calculating  $ds$ .

increment  $ds$  is not  $dr$  in the lab frame, but is rather an increment of distance a photon travels within the wind itself. Consider a direction  $\theta$  with respect to the line of sight, an increment in the line of sight  $d\tilde{s}$  is related to  $dr$  through  $d\tilde{s} = dr / \cos \theta$  without considering motion of the outflow. When relativistic motion is considered, the propagation factor  $(1 - \beta \cos \theta)$  is introduced (the stretch in distance for the photon to catch up to the ejecta, which is moving close to the speed of light, see Fig. 7.7), so that one has

$$ds = \frac{(1 - \beta \cos \theta)}{\cos \theta} dr. \quad (7.61)$$

As a result, the photosphere radius is a function of  $\theta$ .

What is most relevant is the radius when  $\theta = 0$  (on-beam outflow), in which case

$$ds \simeq (1 - \beta) dr \simeq \frac{dr}{2\Gamma_0^2}. \quad (7.62)$$

Plugging Eqs. (7.60) and (7.62) into Eq. (7.59), one gets

$$\int_{R_{\text{ph}}}^{\infty} \frac{\sigma_T L_w \mathcal{Y}}{8\pi r^2 m_p c^3 \eta \Gamma_0^2} dr = 1. \quad (7.63)$$

At this point, it is useful to compare  $R_{\text{ph}}$  with the coasting radius  $R_c$ . The logic is the following: the acceleration of the ejecta (under its thermal pressure) proceeds fundamentally via electromagnetic interactions. Photons scatter electrons, which in turn drag protons to relativistic speeds. If  $R_{\text{ph}} > R_c$ , the outflow has already reached its maximum achievable Lorentz factor ( $\Gamma_0 = \eta$ ) when photons escape. However, if  $R_{\text{ph}}$  is smaller than the *projected coasting radius*  $R_{c,\text{max}} = R_0 \eta$ , most photons will escape the fireball before the fireball is accelerated to the desired maximum Lorentz factor. The fireball Lorentz factor cannot reach the maximum possible value  $\eta$ , but can rather reach a smaller value  $\Gamma_{\text{ph}} = \Gamma_0 < \eta$ . The transition between these two regimes is defined by the condition  $R_{\text{ph}} = R_c$  (Mészáros and Rees, 2000b), which gives

$$\eta = \eta_* \equiv \left( \frac{L_w \sigma_T \mathcal{Y}}{8\pi m_p c^3 R_0} \right)^{1/4} \simeq 8.7 \times 10^2 \left( \frac{L_{w,52} \mathcal{Y}}{R_{0,7}} \right)^{1/4}. \quad (7.64)$$

The expression of the photosphere radius can then be derived in two regimes (Mészáros and Rees, 2000b):

- $\eta < \eta_*$ : In this regime, the fireball already reaches the coasting phase at the photosphere, so that  $\Gamma_0 = \eta$ . One therefore gets

$$R_{\text{ph}} = \frac{\sigma_{\text{T}} L_w \mathcal{Y}}{8\pi \eta \Gamma_0^2 m_p c^3} = \frac{\sigma_{\text{T}} L_w \mathcal{Y}}{8\pi \eta^3 m_p c^3} \simeq (5.9 \times 10^{12} \text{ cm}) L_{w,52} \mathcal{Y} \eta_2^{-3}. \quad (7.65)$$

Since the observed temperature drops with radius as  $T \propto r^{-2/3}$  (Eq. (7.41)) in the coasting regime, the photosphere temperature in this regime reads

$$T_{\text{ph}} = T_0 \left( \frac{R_{\text{ph}}}{R_c} \right)^{-2/3}, \quad (7.66)$$

where  $T_0$  is defined in Eq. (7.44). Noting that the effective emission radius of the photosphere blackbody emission is  $\sim R_{\text{ph}} / \Gamma_{\text{ph}}$  (i.e. an observer can only see within the  $1/\Gamma_{\text{ph}}$  cone) and that  $\Gamma_{\text{ph}} = \Gamma_0$  (the coasting Lorentz factor), one can derive the *isotropic* photosphere luminosity:

$$\begin{aligned} L_{\text{ph}} &= g_0 \sigma_{\text{B}} T_{\text{ph}}^4 (4\pi) \left( \frac{R_{\text{ph}}}{\Gamma_{\text{ph}}} \right)^2 \\ &= g_0 \sigma_{\text{B}} T_0^4 \left( \frac{R_{\text{ph}}}{R_c} \right)^{-8/3} (4\pi) \left( \frac{R_c}{\Gamma} \right)^2 \left( \frac{R_{\text{ph}}}{R_c} \right)^2 \\ &= g_0 \sigma_{\text{B}} T_0^4 (4\pi) R_0^2 \left( \frac{R_{\text{ph}}}{R_c} \right)^{-2/3} \\ &= L_w \left( \frac{R_{\text{ph}}}{R_c} \right)^{-2/3}, \end{aligned} \quad (7.67)$$

where Eq. (7.44) has been used.

- $\eta > \eta_*$ : In this regime, the fireball does not reach the full Lorentz factor defined by  $\eta$ , but only reaches a Lorentz factor  $\Gamma_0 = R_{\text{ph}}/R_0$ . Solving Eq. (7.63), one can derive the photosphere radius in this regime:

$$R_{\text{ph}} \simeq \left( \frac{L_w \sigma_{\text{T}} \mathcal{Y}}{8\pi m_p c^3 \eta} \right)^{1/3} R_0^{2/3} \simeq (1.8 \times 10^{10} \text{ cm}) L_{w,52}^{1/3} \mathcal{Y}^{1/3} \eta_2^{-1/3} R_{0,7}^{2/3}. \quad (7.68)$$

The photosphere temperature in this regime is

$$T_{\text{ph}} \simeq T_0. \quad (7.69)$$

Similar to the  $\eta < \eta_*$  case, one can also derive

$$L_{\text{ph}} = g_0 \sigma_{\text{B}} T_{\text{ph}}^4 (4\pi) \left( \frac{R_{\text{ph}}}{\Gamma_{\text{ph}}} \right)^2 \simeq g_0 \sigma_{\text{B}} T_0^4 (4\pi) R_0^2 = L_w. \quad (7.70)$$

So, in this regime, the observed photosphere luminosity is essentially the original central engine wind luminosity.

Combining the two regimes, the final properties of the fireball photosphere can be summarized as (Mészáros and Rees, 2000b) (Exercise 7.3)

$$\Gamma_{\text{ph}} = \Gamma_0 = \begin{cases} \eta, & \eta < \eta_*, \\ \eta_*^{4/3} \eta^{-1/3}, & \eta > \eta_*. \end{cases} \quad (7.71)$$

$$R_{\text{ph}} = R_c \begin{cases} \left(\frac{\eta_*}{\eta}\right)^4, & \eta < \eta_*, \\ 1, & \eta > \eta_*. \end{cases} \quad (7.72)$$

$$T_{\text{ph}} = T_0 \begin{cases} \left(\frac{R_{\text{ph}}}{R_c}\right)^{-2/3} = \left(\frac{\eta}{\eta_*}\right)^{8/3}, & \eta < \eta_*, \\ 1, & \eta > \eta_*. \end{cases} \quad (7.73)$$

$$L_{\text{ph}} = L_w \begin{cases} \left(\frac{R_{\text{ph}}}{R_c}\right)^{-2/3} = \left(\frac{\eta}{\eta_*}\right)^{8/3}, & \eta < \eta_*, \\ 1, & \eta > \eta_*. \end{cases} \quad (7.74)$$

### 7.3.4 Deceleration

After the internal shock phase, the residual internal energy of the fireball rapidly decreases due to radiative and adiabatic cooling. At the deceleration radius, one may approximate the fireball as a cold shell with most of the fireball energy in the kinetic form.

#### Deceleration Radius: $R_{\text{dec}}$

Let us consider an impulsive (duration negligible), isotropic fireball with a total energy  $E$  (in the kinetic form), an initial mass  $M_0$ , and an initial Lorentz factor  $\Gamma_0$  being decelerated by a circumburst medium. Denoting the mass collected from the medium as  $m$ , which is a function of radius  $r$  and time (lab-frame time or observer-frame time).

For simplicity, we assume a weak reverse shock (which is true most of the time for an impulsive fireball before the deceleration radius, see §8.7 for details), and consider a relativistic forward shock propagating into the medium. For a certain amount of  $m$ , the total energy in the system before shock propagation is  $E = (\Gamma_0 M_0 + m)c^2$ . After shock crossing it reads  $E = \Gamma(M_0 c^2 + hV) = \Gamma(M_0 c^2 + \hat{\gamma}(\Gamma - 1)mc^2 + mc^2)$ , where  $V$  is the volume that encloses  $m$ , so that  $m = \rho V$  and  $h = e + p + \rho c^2$  is the enthalpy density in the shocked region (which is the relevant quantity in  $T_{00}$  for relativistic hydrodynamics). Noting  $p = (\hat{\gamma} - 1)e$ , and  $e = (\Gamma - 1)\rho c^2$  based on relativistic shock jump conditions (Eq. (4.76)), one may write energy conservation before and after collecting a medium mass  $m$  in the form<sup>6</sup>

$$\Gamma_0 M_0 + m = \Gamma[M_0 + \hat{\gamma}(\Gamma - 1)m + m] \simeq \Gamma(M_0 + \hat{\gamma}\Gamma m), \quad (7.75)$$

where  $\Gamma$  is the Lorentz factor of the blastwave after collecting  $m$ , and  $m \ll M_0$  has been applied.

Deceleration becomes important when the two terms on the right hand side become comparable, i.e.  $M_0 = \hat{\gamma}\Gamma m$ , or the collected mass

$$m_{\text{dec}} = \frac{M_0}{\hat{\gamma}\Gamma_{\text{dec}}} = \frac{2M_0}{\hat{\gamma}\Gamma_0} = \frac{3}{2} \frac{M_0}{\Gamma_0} \sim \frac{M_0}{\Gamma_0}, \quad (7.76)$$

<sup>6</sup> The initial energy of the fireball is  $E = \Gamma_0 M_0 c^2$ . The total energy in the blastwave gradually increases with time (neglecting radiation losses) since the rest mass energy of the medium  $mc^2$  is added to the blastwave. However, since  $m \ll \Gamma_0 M_0$ , the additional energy is negligible.

where

$$\Gamma_{\text{dec}} = \frac{1}{2}\Gamma_0. \quad (7.77)$$

The deceleration radius can be calculated based on the condition (7.76). For a constant density hydrogen medium with proton number density  $n$ , typical for an ISM, the condition reads

$$\frac{4\pi}{3}R_{\text{dec}}^3 n m_p c^2 = \frac{E}{\hat{\gamma}\Gamma_0\Gamma_{\text{dec}}} = \frac{2E}{\hat{\gamma}\Gamma_0^2}. \quad (7.78)$$

This gives the deceleration radius

$$R_{\text{dec}}(\text{ISM}) = \left( \frac{3E}{2\pi\hat{\gamma}\Gamma_0^2 n m_p c^2} \right)^{1/3} \simeq (6.2 \times 10^{16} \text{ cm}) E_{52}^{1/3} \Gamma_{0,2}^{-2/3} n^{-1/3}, \quad (7.79)$$

where  $\hat{\gamma} = 4/3$  has been adopted in deriving the numerical coefficient. Hereafter when the afterglow problem is discussed,  $E = E_{K,\text{iso}}$  stands for the total isotropic kinetic energy in the fireball.

The observed deceleration time scale can be calculated through

$$\begin{aligned} t_{\text{dec}}(\text{ISM}) &= \int_0^{R_{\text{dec}}} \frac{(1+z)dr}{2[\Gamma(r)]^2 c} \simeq 0.9(1+z) \frac{R_{\text{dec}}}{\Gamma_0^2 c} \\ &\simeq (370 \text{ s}) E_{52}^{1/3} \Gamma_{0,2}^{-8/3} n^{-1/3} \left( \frac{1+z}{2} \right), \end{aligned} \quad (7.80)$$

where the coefficient 0.9 is derived from numerical integration for a constant density medium (Exercise 7.4). Observationally, assuming that the peak time of optical afterglow is the deceleration time, one can derive the initial Lorentz factor of the fireball for the ISM model:

$$\begin{aligned} \Gamma_0(\text{ISM}) &\simeq 0.9^{3/8} \left( \frac{3E(1+z)^3}{2\pi\hat{\gamma} n m_p c^5 t_{\text{dec}}^3} \right)^{1/8} \\ &\simeq 170 t_{\text{dec},2}^{-3/8} \left( \frac{1+z}{2} \right)^{3/8} E_{52}^{1/8} n^{-1/8}. \end{aligned} \quad (7.81)$$

In GRB problems, a stellar wind medium is also considered for the massive star progenitor of long GRBs. The reasoning is that the massive star progenitor may have ejected a continuous wind before dying, so that the circumburst medium is modified by the wind.

Let us assume a stellar wind with constant mass loss rate  $\dot{M}_w$  and constant wind speed  $V_w$ . The density of the wind is therefore (Chevalier and Li, 2000)

$$\rho = \frac{\dot{M}_w}{4\pi r^2 V_w} = A r^{-2} = (5 \times 10^{11} \text{ g cm}^{-1}) A_* r^{-2}, \quad (7.82)$$

where

$$A_* = \frac{A}{5 \times 10^{11} \text{ g cm}^{-1}}. \quad (7.83)$$



Assuming a hydrogen stellar wind, the proton/electron number density is

$$n = \frac{\rho}{m_p} \simeq (3.0 \times 10^4 \text{ cm}^3) A_* r_{15}^{-2}. \quad (7.84)$$

Again for an impulsive fireball, the deceleration dynamics give (Exercise 7.4)

$$R_{\text{dec}}(\text{wind}) = \frac{E}{2\pi \hat{\gamma} A \Gamma_0^2 c^2} \simeq (2.7 \times 10^{14} \text{ cm}) E_{52} A_*^{-1} \Gamma_2^{-2}, \quad (7.85)$$

and the deceleration time is

$$\begin{aligned} t_{\text{dec}}(\text{wind}) &= \int_0^{R_{\text{dec}}} \frac{(1+z)dr}{2[\Gamma(r)]^2 c} \simeq 1.3(1+z) \frac{R_{\text{dec}}}{\Gamma_0^2 c} \\ &\simeq (1.8 \text{ s}) \left( \frac{1+z}{2} \right) E_{52} A_*^{-1} \Gamma_{0,2}^{-4}. \end{aligned} \quad (7.86)$$

In terms of the deceleration time, the bulk Lorentz factor is

$$\begin{aligned} \Gamma_0(\text{wind}) &\simeq 1.3^{1/4} \left( \frac{E(1+z)}{2\pi \hat{\gamma} A c^3 t_{\text{dec}}} \right)^{1/4} \\ &\simeq 120 t_{\text{dec}}^{-1/4} \left( \frac{1+z}{2} \right)^{1/4} E_{52}^{1/4} A_*^{-1/4}. \end{aligned} \quad (7.87)$$

One can see that the typical deceleration time is much shorter than in the ISM case due to the much higher density in a wind environment. Unless the wind parameter  $A_*$  is much smaller than unity, this time is usually shorter than the duration of the GRB. The impulsive assumption is no longer valid, and one needs to consider the thick shell regime, as discussed below. The estimate of  $\Gamma_0$  for the wind case (Eq. (7.87)) is also only valid when the impulsive condition (thin shell regime) is satisfied.

### Thin and Thick Shells

At this point, it is appropriate to introduce the concepts of “thin” and “thick” shells (Sari and Piran, 1995).

A *thin shell* means that the fireball shell is thin enough so that the spreading radius is smaller than the deceleration radius, or the duration of the burst,  $T_{\text{GRB}}$ , is shorter than the deceleration time scale defined above, i.e.

$$\Gamma_0^2 \Delta_0 < R_{\text{dec}} \quad (7.88)$$

or

$$T_{\text{GRB}} < \frac{R_{\text{dec}}}{\Gamma_0^2 c} \sim t_{\text{dec}}. \quad (7.89)$$

In this regime, the thickness of the shell does not enter the problem, and the fireball is effectively an “impulsive” one. The above derivations of the deceleration radii and times apply to this regime.

A *thick shell* refers to the opposite case, i.e.

$$\Gamma_0^2 \Delta_0 > R_{\text{dec}} \quad (7.90)$$

or

$$T_{\text{GRB}} > \frac{R_{\text{dec}}}{\Gamma_0^2 c} \sim t_{\text{dec}}. \quad (7.91)$$

In this case, the entire shell is not fully decelerated at the above-defined radii. The true deceleration radius is located where the reverse shock crosses the entire ejecta. This is roughly at

$$R_{\text{dec}}^{\text{thick}} \simeq \Gamma_0^2 \Delta_0. \quad (7.92)$$

The above derived deceleration radius (Eq. (7.79)) and time (Eq. (7.80)) are not relevant.

### Sedov Radius: $R_{\text{Sedov}}$ or $l$

A decelerating fireball will eventually enter the *non-relativistic* or *Newtonian* phase. This radius is called the *Sedov radius*, which is where the medium energy collected in the fireball becomes comparable to the initial energy of the fireball, i.e.

$$\frac{4\pi}{3} R_{\text{Sedov}}^3 n m_p c^2 = E. \quad (7.93)$$

This gives the Sedov radius

$$R_{\text{Sedov}}(\text{ISM}) \equiv l(\text{ISM}) \equiv \left( \frac{3E}{4\pi n m_p c^2} \right)^{1/3} \simeq (1.2 \times 10^{18} \text{ cm}) (E_{52}/n)^{1/3}. \quad (7.94)$$

The corresponding time (both lab frame and observer frame since the two times have little difference when the fireball enters the Newtonian regime) is

$$t_{\text{NR}}(\text{ISM}) \simeq l(\text{ISM})/c \simeq (450 \text{ days}) (E_{52}/n)^{1/3}. \quad (7.95)$$

Notice that the above Sedov radius is defined using the isotropic energy of the fireball. Livio and Waxman (2000) suggested that if significant sideways expansion occurs, one should use the beaming-corrected jet energy  $E_j$  to define the radius, so that the transition time to the Newtonian phase is significantly earlier. Numerical simulations (Zhang and MacFadyen, 2009) suggested that sideways expansion is not important, so that the fireball is still relativistic at the epoch defined by Livio and Waxman (2000). According to these simulations, the above-defined  $t_{\text{NR}}$  is indeed roughly consistent with the time of Newtonian phase transition.

A similar Newtonian radius can be derived for the case of a wind medium, which reads (Exercise 7.5)

$$R_{\text{Sedov}}(\text{wind}) \equiv l(\text{wind}) \equiv \frac{E}{4\pi A c^2} \simeq (1.8 \times 10^{18} \text{ cm}) E_{52} A_*^{-1}. \quad (7.96)$$

A stellar wind will eventually interact with the ISM, forming a pair of wind termination shocks. Beyond the forward termination shock, the density profile resumes the constant profile as expected in an ISM. The radius of the forward termination shock depends on

the wind mass loss rate and the age of the star, which reads (Castor et al., 1975; Pe'er and Wijers, 2006)

$$R_{\text{FS},w} = \left( \frac{125}{308\pi} \right)^{1/5} \left( \frac{\dot{M}_w v_w^2 t_*^3}{\rho_{\text{ISM}}} \right)^{1/5} = (1.6 \times 10^{19} \text{ cm}) \dot{M}_{w,-6}^{1/5} v_{w,8}^{2/5} n_{0,3}^{-1/5} t_{*,6}^{3/5}, \quad (7.97)$$

where  $\dot{M}_w = (10^{-6} M_\odot \text{ yr}^{-1}) \dot{M}_{w,-6}$  is the mass loss rate,  $v_w = (10^8 \text{ cm s}^{-1}) v_{w,8}$  is the wind speed (this combination of  $\dot{M}_w$  and  $v_w$  corresponds to  $A = \dot{M}_w / 4\pi v_w \simeq 5 \times 10^{10} \text{ g cm}^{-1}$ , or  $A_* = 0.1$ ), and  $t_* = (10^6 \text{ yr}) t_{*,6}$  is the lifetime of the Wolf–Rayet phase of the star. The radius of the reverse termination shock is defined by balancing the wind ram pressure and the shocked ISM pressure, which reads (Pe'er and Wijers, 2006)

$$R_{\text{RS},w} = \left( \frac{3 \dot{M}_w v_w}{4 4\pi P_b} \right)^{1/2} = (1.6 \times 10^{18} \text{ cm}) \dot{M}_{w,-6}^{3/10} v_{w,8}^{1/10} n_{0,3}^{-3/10} t_{*,6}^{2/5}, \quad (7.98)$$

where  $P_b = (7/25)(125/308\pi)^{2/5} \rho_{\text{ISM}} (\dot{M}_w v_w^{2/5} / \rho_{\text{ISM}} t_*^2)^{2/5}$  is the pressure in the shocked wind (also shocked ISM) region.

One can see that for typical parameters (e.g.  $E_{52} = 1$ ,  $A_* = 1$ ),  $R_{\text{RS},w}$  is comparable to  $l(\text{wind})$ . In a large parameter space (e.g.  $E_{52} \geq 1$  or  $A_* \leq 1$ ),  $R_{\text{RS},w}$  is smaller than  $l(\text{wind})$ . The Sedov length in the wind case (Eq. (7.96)) is therefore not relevant in these cases.

When the blastwave reaches the wind termination shock regions, interesting observational signatures are expected. These have been investigated by a number of authors (Ramirez-Ruiz et al., 2001; Dai and Lu, 2002; Dai and Wu, 2003; Ramirez-Ruiz et al., 2005; Pe'er and Wijers, 2006).

### 7.3.5 Neutrons in the Fireball

The fireball in the discussion so far is composed only of photons, pairs, and protons. In most central engine models, neutrons are expected to be launched in the jet together with protons (Derishev et al., 1999; Beloborodov, 2003b). The central engine is usually too hot and too dense for nuclei to survive. They are expected to be dissociated. The collapsar central engine is rich in neutrons when the Fe core is dissociated. A compact star merger invokes disruption of at least one neutron star, so that the engine is naturally neutron rich. As a result, the baryons launched in a hot fireball jet are expected to be mostly in the form of free protons and neutrons, even though some marginal nucleosynthesis might occur (Lemoine, 2002; Beloborodov, 2003b).

In a neutron-rich fireball, free neutrons are initially coupled with protons through elastic nuclear scattering with an optical depth

$$\tau_{pn} = \sigma_{pn} n'_p v' \simeq \sigma_{pn,0} n'_p c, \quad (7.99)$$

where  $v'$  is the mean value of the kinetic relative velocity of protons and neutrons in the comoving frame,  $n'_p$  is the comoving proton number density, and the scattering cross section above 0.1 MeV and below the pion production threshold 140 MeV may be approximated as

$$\sigma_{pn}(v) = \sigma_{pn,0}(c/v), \quad (7.100)$$

with  $\sigma_{pn,0} \simeq 3 \times 10^{-26} \text{ cm}^2$ .

Protons and neutrons decouple at a distance where  $\tau_{pn} < 1$  is satisfied. Beyond this distance, neutrons stream freely, independent of protons. Whether neutrons and protons will coast with the same Lorentz factor depends on whether the energy-to-mass ratio  $\eta$  of the fireball is large enough to allow  $np$  decoupling before the protons reach the maximum Lorentz factor. The treatment is similar to that of the photosphere (for which photon–electron scatterings are considered) as discussed in §7.3.3, with the Thomson cross section  $\sigma_T$  replaced by  $\sigma_{pn,0}$ .

Let us define

$$\xi = \frac{n_n}{n_p}, \quad (7.101)$$

so that the fraction of protons in the fireball is  $1/(1 + \xi)$ . Still defining  $\eta = L_w/\dot{M}c^2$ , one can define a critical value of  $\eta$  (Mészáros and Rees, 2011)<sup>7</sup>

$$\eta_{pn} = \left[ \frac{L_w \sigma_{pn,0}}{8\pi m_p c^3 R_0 (1 + \xi)} \right]^{1/4} \simeq 4.0 \times 10^2 L_{w,52}^{1/4} R_{0,7}^{-1/4} (1 + \xi)^{-1/4}. \quad (7.102)$$

Re-defining (cf. Eq. (7.64))

$$\eta_* = \left[ \frac{L_w \sigma_T}{8\pi m_p c^3 R_0 (1 + \xi)} \right]^{1/4} \simeq 8.7 \times 10^2 L_{w,52}^{1/4} R_{0,7}^{-1/4} (1 + \xi)^{-1/4}, \quad (7.103)$$

one can obtain

$$\eta_{pn} = \eta_* \left( \frac{\sigma_{pn,0}}{\sigma_T} \right)^{1/4} \simeq 0.46 \eta_*. \quad (7.104)$$

For  $\eta < \eta_{pn}$ , neutrons and protons are coupled before the entire outflow reaches the maximum Lorentz factor. For  $\eta > \eta_{pn}$ , on the other hand, neutrons decouple from protons at  $\eta_{pn}$  before protons reach the maximum Lorentz factor  $\min(\eta, \eta_*)$ . There is a relative velocity between protons and neutrons. The interaction between protons and neutrons would produce 5–10 GeV neutrinos through inelastic  $pn$  interactions (§6.2.3) (Bahcall and Mészáros, 2000).

Since neutrons are neutral, they are not subject to electromagnetic interactions. For a variable outflow, whereas proton shells collide and produce internal shocks, neutron shells can stream through each other and also through proton shells freely, essentially without energy dissipation from internal shocks. However, they can interact with the proton shells to produce neutrinos if the inelastic  $pn$  interaction threshold (pion production threshold 140 MeV) is reached (even if for  $\eta < \eta_{pn}$ ).

Free neutrons eventually go through  $\beta$ -decay

$$n \rightarrow p + e^- + \bar{\nu}_e, \quad (7.105)$$

with a mean comoving lifetime of just under 15 minutes, i.e.

$$\tau'_n = 881.5 \pm 1.5 \text{ s} \sim 900 \text{ s}. \quad (7.106)$$

<sup>7</sup> The factor  $4\pi$  in Eq. (1) of Mészáros and Rees (2011) is replaced by  $8\pi$  for a more precise treatment. See §7.3.3 for the derivation of the  $8\pi$  parameter.

Once they decay, the newly formed decay products (protons and electrons) immediately participate in all the interactions (shock, acceleration, radiation, etc.). The typical radius of neutron decay is

$$R_\beta = c\tau'_n\Gamma_n \simeq (8 \times 10^{15} \text{ cm})(\Gamma_n/300). \quad (7.107)$$

This is a radius slightly below the deceleration radius. Since neutron decay happens continuously in time (and in distance), neutron decay inevitably affects radiation signatures in both prompt emission and early afterglow phase. These effects will be further discussed later in §8.8.1 and §9.9.4.

## 7.4 Poynting-Flux-Dominated Jet

Another extreme for the GRB ejecta composition is the Poynting-flux-dominated regime ( $\sigma \gg 1$ ). The jet dynamics are significantly different from the fireball case. Since the thermal component is negligible in this regime, the generalized magnetization parameter (Eq. (7.26)) is reduced to (no thermal energy, i.e.  $\Theta = 1$ )

$$\sigma \equiv \frac{B^2}{4\pi\Gamma\rho c^2} = \frac{B'^2}{4\pi\rho'c^2}, \quad (7.108)$$

where  $B$  and  $\rho$  are magnetic field strength and matter density in the lab frame, and  $B'$  and  $\rho'$  are the corresponding quantities in the comoving frame.

### 7.4.1 Magnetic Field Configurations

In contrast to the fireball scenario for which isotropy is a good approximation of the problem, a Poynting-flux-dominated outflow carries a globally ordered magnetic field, so that the problem is intrinsically anisotropic.

The evolution of a Poynting-flux-dominated jet is affected by the magnetic field configuration. One important fact is that the GRB central engine (a hyper-accreting black hole, or a millisecond magnetar) must be spinning rapidly. As a result, a realistic GRB jet model must introduce a strong toroidal magnetic field component.

The field configuration depends on whether the magnetic axis is aligned with the spin axis, which determines whether the system is *axisymmetric* or *non-axisymmetric*. In the following, we will discuss three magnetic field configurations: *helical*, *striped wind* (Spruit et al., 2001), and self-confined magnetic blobs (Li et al., 2006).

### Helical Geometry

The first “helical” configuration arises when the magnetic field axis aligns with the spin axis of the system. In this configuration, the system is roughly axisymmetric (Fig. 7.8). The configuration is relevant for a hyper-accreting black hole with a prograde accretion disk or torus without significant precession. In such a system, the magnetic field lines are

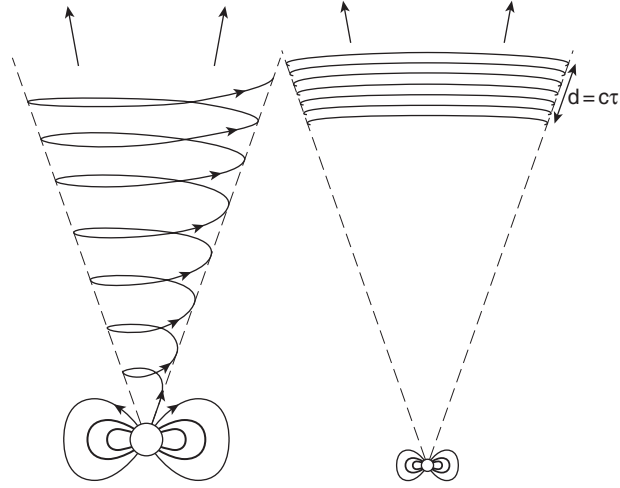


**Figure 7.8** The helical magnetic configuration in GRB jets. From Spruit et al. (2001).

expected to be roughly axisymmetric with respect to the axis of the accretion disk, which is also likely the direction of the black hole spin. One may also call such a magnetic field configuration *black-hole-like*.

A magnetic configuration of this type may be achieved when an axisymmetric poloidal field is wrapped around the jet axis into an azimuthal field configuration. This would give rise to a “helical” configuration, as shown in the left panel of Fig. 7.8. Since the GRB central engine duration is short, typically tens to hundreds of seconds, the end of the jet detaches from the central engine when the front of the jet reaches a distance of  $d \sim cT_{\text{GRB}} = 3 \times 10^{12} \text{ cm} T_{\text{GRB},2}$ . When emission occurs at a large radius (say,  $R_\gamma \sim \Gamma^2 c \Delta t = (3 \times 10^{14} \text{ cm}) \Gamma_2^2 \Delta t$ ), the so-called “jet” is already far away from the central engine, which looks like a “flying pancake” with wrapped wires (right panel of Fig. 7.8).

### Striped-Wind Geometry

The second configuration is the “striped-wind” geometry. This arises when the magnetic field axis is mis-aligned with the spin axis, similar to the case in pulsars. Such a configuration may also be called *pulsar-like*. It may be relevant for a millisecond magnetar central engine.

As seen in Fig. 7.9, the outflow from such a system is quasi-spherical driven by a perpendicular rotator. Viewing in the equatorial direction (left panel of Fig. 7.9), one can see a striped wind with layers of alternating magnetic polarity of a characteristic width of  $\sim cP$ , where  $P$  is the period of the millisecond rotator. This is because the field lines originating from opposite poles enter or exit the paper plane due to the rapid rotation. Viewed from the pole of rotation (middle panel of Fig. 7.9), one can see two wrapped spiral field lines with opposite orientations forming “stripes”. At large radii where emission happens (right panel of Fig. 7.9), the field lines are concentrated in a thin spherical shell, with the cross section in the equatorial plane mimicking concentric rings.

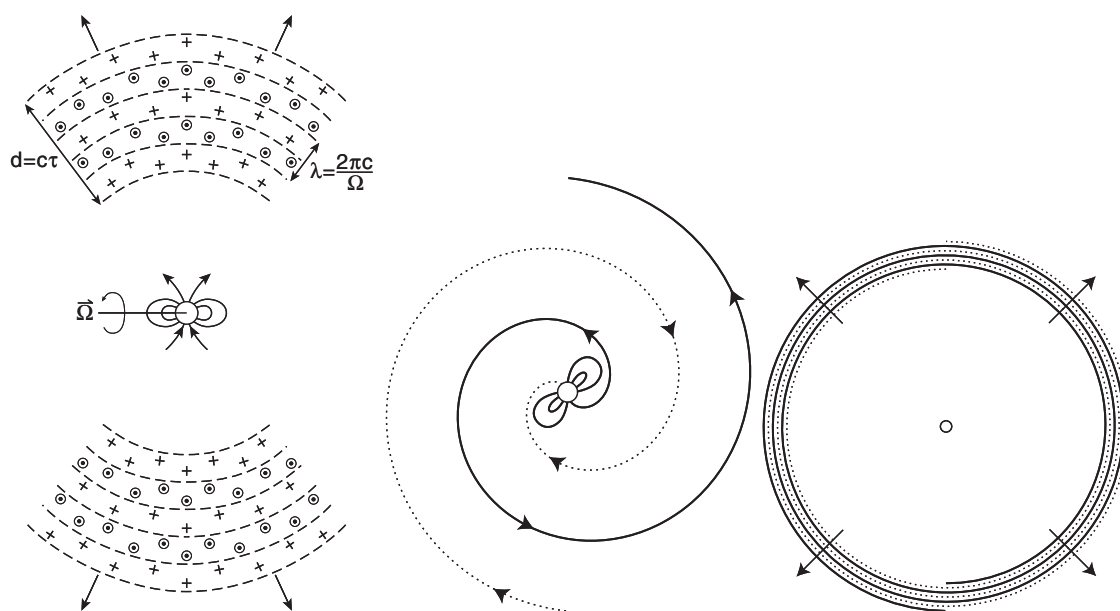


**Figure 7.9** The striped-wind magnetic configuration in GRB jets. From Spruit et al. (2001).

For a millisecond magnetar born during the core collapse of a massive star, numerical simulations show that the magnetar outflow tends to be collimated along the rotation axis of the collapsing star (Bucciantini et al., 2009). A collimated jet similar to the helical case would be launched, but with a striped-wind geometry (alternating field-line directions). The magnetic jet of such a configuration is more likely subject to dissipation compared to the helical configuration, since reconnections occur more easily due to the existence of striped magnetic field lines with alternating polarity in the ejecta.

### Magnetic Blobs

When a GRB “jet” is detached from the central engine, the magnetic field lines may lose contact with the engine. If this outflow is collimated into a small solid angle, as is expected from the “collapsar” scenario of long GRBs, a magnetically self-confined *magnetic blob* may be formed. There are several reasons to envisage the existence of such blobs. First of all, due to the short nature of GRBs, when the high- $\sigma$  central engine wind stops, the Poynting-flux-dominated ejecta will be detached from the engine, so that a self-closed magnetic system will be formed. In a sense, the entire ejecta may be treated as a large blob. Furthermore, within the ejecta, smaller blobs may form due to the intrinsic *episodic* nature of the central engine, e.g. due to unsteady accretion (e.g. Perna et al., 2006; Proga and Zhang, 2006), episodic ejection of magnetic loops from a differentially rotating disk or torus (e.g. Yuan and Zhang, 2012), current-driven kink instability (e.g. Mizuno et al., 2012), or magnetic activities from a newborn, differentially rotating neutron star central engine (e.g. Kluźniak and Ruderman, 1998; Dai et al., 2006).

There exists a mathematical model to describe such a self-closed magnetic blob configuration with both poloidal and toroidal components (Li et al., 2006). Writing in a cylindrical coordinate system  $(r, \phi, z)$ , one may introduce an axisymmetric poloidal flux function

$$\Phi(r, z) = B_{b,0} r^2 \exp\left(-\frac{r^2 + z^2}{r_0^2}\right), \quad (7.109)$$

where  $B_{b,0}$  and  $r_0$  are normalization factors for the strength and characteristic scale of the magnetic blob. The poloidal field can be calculated as

$$B_r = -\frac{1}{r} \frac{\partial \Phi}{\partial z} = 2B_{b,0} \frac{zr}{r_0^2} \exp\left(-\frac{r^2 + z^2}{r_0^2}\right), \quad (7.110)$$

$$B_z = -\frac{1}{r} \frac{\partial \Phi}{\partial r} = 2B_{b,0} \left(1 - \frac{r^2}{r_0^2}\right) \exp\left(-\frac{r^2 + z^2}{r_0^2}\right), \quad (7.111)$$

which is closed, with the global net poloidal flux being zero. The toroidal component may be delineated

$$B_\phi = \frac{\alpha \Phi}{r} = B_{b,0} \alpha r \exp\left(-\frac{r^2 + z^2}{r_0^2}\right), \quad (7.112)$$

where the parameter  $\alpha$  stands for the ratio between the toroidal and poloidal flux. Li et al. (2006) showed that when the poloidal and toroidal fluxes are comparable, the value of  $\alpha$  is  $\sim 2.6$ . Figure 7.10 shows an example of magnetic field lines of such a magnetic blob with a high toroidal-to-poloidal ratio.

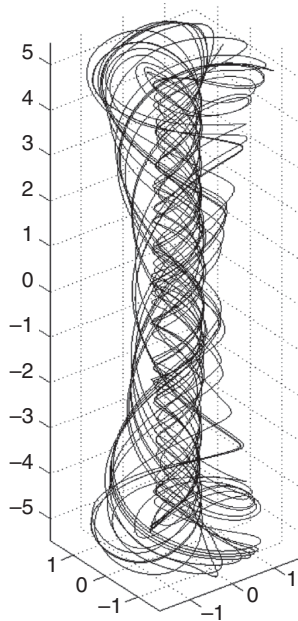


**Figure 7.10**

An example of magnetic configuration in a self-confined magnetic blob. Reproduced from Figure 7 in Li et al. (2006) with permission. ©AAS.



## Poloidal vs. Toroidal Fields

If one neglects magnetic dissipation, the magnetic flux should be conserved as the jet expands in space. For a poloidal configuration, flux conservation demands  $B_p r^2 \simeq \text{const}$ , or

$$B_p \propto r^{-2}. \quad (7.113)$$

For a toroidal configuration, on the other hand, the field lines are in the plane perpendicular to the jet motion direction. If the jet moves with a constant speed (Lorentz factor), i.e. no energy transfer from the Poynting flux energy to kinetic energy, then the Poynting flux energy ( $\propto B_\phi^2/(4\pi)V_j$ ) should be conserved. The volume of the jet is  $V_j \propto r^2 \Delta$ . If the width of the shell  $\Delta$  essentially remains unchanged, one can write  $B_\phi^2 r^2 \simeq \text{const}$ , or

$$B_\phi \propto r^{-1}. \quad (7.114)$$

As a result,  $B_p$  decays much faster with  $r$  than does  $B_\phi$ . In the GRB problem, the emission radius is usually much larger than the central engine radius, i.e.  $R_{\text{GRB}}/R_0 \gg 1$ . As a result, in the emission region, the magnetic field configuration may be *toroidally dominated*.

### 7.4.2 Magnetic Acceleration

A magnetically dominated jet can be self-accelerated. This happens even in the ideal MHD regime without magnetic dissipation, due to the non-zero magnetic pressure gradient existing within the outflow. This mechanism has been widely discussed within the content of pulsar winds, AGN jets (e.g. Michel, 1969; Goldreich and Julian, 1970; Li et al., 1992; Komissarov et al., 2007), and GRB jets (e.g. Vlahakis and Königl, 2003; Komissarov et al., 2009; Granot et al., 2011).

When magnetic fields are dissipated within the outflow (e.g. due to reconnection), a fraction of magnetic energy is deposited as thermal energy and then gets converted into kinetic energy. This gives additional acceleration to the outflow.

## The MHD Condition

In GRB problems, an MHD approximation is usually made. Below we outline the physical condition for an MHD approximation, and justify that the condition is satisfied for most of the problems we are studying. Discussion of the MHD condition can be found in e.g. Spruit et al. (2001), Zhang and Mészáros (2002a), and Drenkhahn and Spruit (2002).

A fluid description of the magnetized ejecta requires that the plasma is frozen in the magnetic fields (Usov, 1994). The minimum charge number density to satisfy this frozen-in condition is the *Goldreich–Julian* (GJ) density  $n_{\text{GJ}} = \mathbf{\Omega} \cdot \mathbf{B}/2\pi ec$ , which is the charge density that sustains corotation of the magnetosphere (Goldreich and Julian, 1969). For a rapidly rotating, highly magnetized object, the GJ density drops as  $\propto r^{-3}$  (since the dipole field strength drops as  $r^{-3}$ ) within the *light cylinder* radius ( $R_{\text{lc}} = c/\Omega$ , where  $\Omega = 2\pi/P$  is the angular velocity, and  $P$  is the rotation period of the central object), but as  $\propto r^{-1}$  (the toroidal magnetic field decay law) beyond the light cylinder radius. Since the GRB central

engines are millisecond rotators,  $R_{lc}$  is typically small, and the emission radius is usually much larger than  $R_{lc}$ . The GJ density can then be estimated as

$$n_{GJ} \sim \left( \frac{\Omega B_*}{2\pi ec} \right) \left( \frac{R_*}{R_{lc}} \right)^3 \left( \frac{R_{lc}}{r} \right) = \frac{B_* R_*^3 \Omega^3}{2\pi ec^3 r}, \quad (7.115)$$

where  $R_*$  is the radius of the central engine (radius of the neutron star or the innermost radius of the accretion disk) and  $B_*$  is the magnetic field strength at the central engine. For a Poynting-flux-dominated outflow, the wind luminosity is essentially the dipole spindown luminosity, i.e.

$$L_w = \frac{B_*^2 R_*^6 \Omega^4}{6c^3}. \quad (7.116)$$

As a result, the lab-frame GJ density at radius  $r$  can be expressed as

$$n_{GJ} = (1.0 \times 10^{10} \text{ cm}^{-3}) L_{w,52}^{1/2} P_{-3}^{-1} r_{13}^{-1}, \quad (7.117)$$

where the spin period is normalized to milliseconds ( $P_{-3}$ ) and the emission radius is normalized to  $10^{13}$  cm.

Suppose that the outflow is loaded with baryons. The lab-frame baryon density, which is also the lab-frame baryon-associated electron density, reads

$$n_b = n_e = \frac{L_w}{4\pi(1+\sigma)r^2 c \Gamma m_p c^2} \simeq (1.8 \times 10^{15} \text{ cm}^{-3}) L_{w,52} (1+\sigma)^{-1} \Gamma_2^{-1} r_{13}^{-2}, \quad (7.118)$$

where  $\sigma$  and  $\Gamma$  are the magnetization parameter and Lorentz factor at radius  $r$ , respectively.

Noticing  $n_{GJ} \propto r^{-1}$  and  $n_e \propto r^{-2}$ , one can draw the conclusion

$$n_e > n_{GJ}, \quad (7.119)$$

i.e. the MHD condition is satisfied, as long as

$$r < R_{\text{MHD}} \equiv (1.8 \times 10^{18} \text{ cm}) L_{w,52}^{1/2} (1+\sigma)^{-1} P_{-3} \Gamma_2^{-1}, \quad (7.120)$$

where  $R_{\text{MHD}}$  is derived by requiring  $n_{GJ} = n_e$ . For typical parameters,  $R_{\text{MHD}}$  is greater than  $R_{\text{dec}}$  (unless  $\sigma$  at such a large radius is still large, which demands an extremely large  $\sigma_0$ ). For realistic GRB problems, the MHD condition is satisfied, and one can apply the MHD approximation to delineate the evolution of the GRB jet.

### Rapid Acceleration Phase

Since the central engine is rapidly spinning and since magnetic fields are attached to the engine, strong toroidal magnetic fields are continuously built up near the engine. Similar to a strongly wound spring, the twisted magnetic fields store strong tension from the magnetic field pressure gradient, continuously accelerating the ejecta forward.

In order for the front part of the jet to receive a push from the back (which is connected to the rapidly rotating central engine), sound waves should have time to propagate across the ejecta and reach the front. This poses an important limit on the bulk Lorentz factor of the outflow.

For a cold (thermal energy negligible), Poynting-flux-dominated outflow, the fast magneto-sonic (ms) wave has a speed similar to the Alfvén speed, both are relativistic, i.e.  $v_F \simeq v_A \sim c$ , and  $\gamma_F \simeq \gamma_A = (1 + \sigma)^{1/2}$  (Eq. (4.111), §4.2.4). The condition for the fast magneto-sonic wave to catch up to the ejecta is therefore  $\gamma_A \geq \Gamma$ , where  $\Gamma$  is the bulk Lorentz factor of the outflow.

Recalling Eq. (7.27), taking  $\eta = 1$  and  $\Theta = 1$ , one has

$$\mu_0 = (1 + \sigma_0) = \Gamma(1 + \sigma) \quad (7.121)$$

during the acceleration phase. Letting  $\Gamma = \gamma_A = \sqrt{1 + \sigma}$  (Eq. (4.109)) at a radius denoted  $R_{\text{ms}}$ , one gets the relation

$$(1 + \sigma_{\text{ms}})^{3/2} = (1 + \sigma_0), \quad (7.122)$$

and

$$\Gamma_{\text{ms}} = (1 + \sigma_{\text{ms}})^{1/2} = (1 + \sigma_0)^{1/3} \simeq \sigma_0^{1/3}. \quad (7.123)$$

The last approximation applies for  $\sigma_0 \gg 1$ . This is the maximum Lorentz factor the ejecta can achieve in a rapid acceleration process via fast magneto-sonic waves. This condition, which is also known as the *sonic condition*, has been derived rigorously within various contexts (Michel, 1969; Goldreich and Julian, 1970; Li et al., 1992; Granot et al., 2011; Kumar and Zhang, 2015). The above short derivation catches the essence of the key physics behind the complicated MHD equations.

### Acceleration Beyond the Sonic Point

Equation (7.121) suggests that the ultimate Lorentz factor a Poynting-flux-dominated jet can reach is  $\Gamma_{\text{max}} = 1 + \sigma_0$  (when  $\sigma \ll 1$  is achieved). At the end of the rapid acceleration (denoted by “ra”) phase at the sonic point, the Lorentz factor is only  $\Gamma_{\text{ra}} = \Gamma_{\text{ms}} = (1 + \sigma_0)^{1/3}$ , so the jet has great potential to keep accelerating. However, beyond the sonic point, acceleration of a magnetized jet becomes difficult and fragile. In the case of a radial wind, it has been shown that the wind can no longer accelerate since the magneto-sonic point is essentially at infinity (Michel, 1969; Goldreich and Julian, 1970). Li et al. (1992) discovered that, if the field lines diverge faster than radially, the fast magneto-sonic point moves from infinity to a much closer distance, so that the outflow can still be accelerated beyond the magneto-sonic point to become *super-magneto-sonic*. The converging of magnetic flux is known as the *magnetic nozzle* effect, since it mimics a gas nozzle. Li et al. (1992) discovered a self-similar solution which demands a special magnetic field configuration. Considering a Poynting-flux-dominated jet propagating inside a progenitor star, Tchekhovskoy et al. (2009) found that the confinement of the jet within the star would facilitate jet acceleration, so that the asymptotic value of  $\Gamma$  increases by a factor of  $\theta_j^{-2/3}$  when the jet exits the star, where  $\theta_j$  is the asymptotic half-opening angle of the jet. Nonetheless, the jet stops accelerating after escaping the star without reaching the maximum value  $(1 + \sigma_0)$ .

Continuous acceleration of the jet to achieve the maximum potential may be achieved in two ways.

Drenkhahn (2002) and Drenkhahn and Spruit (2002) introduced a continuous magnetic dissipation scenario. Within this scenario, magnetic dissipation continuously occurs at all radii, likely through magnetic reconnection in a striped magnetic wind. Through solving relativistic MHD equations and introducing a prescription for magnetic dissipation, Drenkhahn (2002) derived a scaling law

$$\Gamma \propto r^{1/3}. \quad (7.124)$$

The essence of this derivation was sketched by Mészáros and Rees (2011), which we highlight here.

Above the magneto-sonic point ( $r > R_{\text{ra}} = R_{\text{ms}}$ ), without additional external pressure confinement, one would have no acceleration, i.e.  $\Gamma(r) = \Gamma_{\text{ms}} = \text{const}$ . Assuming a constant comoving-frame reconnection speed  $v'_r$ , one has the comoving-frame reconnection time  $t'_r = \lambda'/v'_r = \Gamma\lambda/v'_r \propto \Gamma$ , where  $\lambda \sim cP$  is the lab-frame spacing between the magnetic “stripes”, which in the comoving frame is larger by a factor  $\Gamma$ . The comoving dynamical time scale is  $t'_{\text{dyn}} \sim r/\Gamma$ . The density of the internal energy due to dissipation (which is used to accelerate the outflow) is  $\Theta \propto t'_r/t'_{\text{dyn}} \propto \Gamma^2/r$ . Assuming  $\Gamma\Theta \propto \Gamma^3/r \sim \text{const}$ , one gets Eq. (7.124). This derivation does not explicitly introduce the  $(1 + \sigma)$  factor in the dynamical evolution.

Granot et al. (2011) used a completely different argument and arrived at similar scaling (7.124) without introducing magnetic dissipation. They pointed out that, when one drops the continuous jet assumption and considers an impulsive magnetically dominated pulse (which is valid for GRBs), the magnetic pressure gradient within the shell can be maintained, so that the front of the shell is continuously accelerated. According to Eq. (7.121), the terminating Lorentz factor should be

$$\Gamma_{\text{max}} \sim 1 + \sigma_0. \quad (7.125)$$

For an impulsive pulse undergoing acceleration, the lab-frame width remains unchanged. Let the shell width be  $\Delta = R_{\text{ms}}$ . At the coasting radius  $R_c$  where Eq. (7.125) is satisfied the width is  $\Delta \sim R_c/\Gamma_{\text{max}}^2 = R_c/(1 + \sigma_0)^2$ ; one therefore has

$$R_c \sim (1 + \sigma_0)^2 R_{\text{ms}}. \quad (7.126)$$

Noting Eqs. (7.122) and (7.123), one can derive the acceleration index

$$\frac{d \log \Gamma}{d \log r} = \frac{\log[\Gamma(R_c)/\Gamma(R_{\text{ms}})]}{\log(R_c/R_{\text{ms}})} = \frac{\log(1 + \sigma_0)^{2/3}}{\log(1 + \sigma_0)^2} = \frac{1}{3}, \quad (7.127)$$

so that Eq. (7.124) is satisfied.

From Eq. (7.27), one can also derive

$$(1 + \sigma) \propto r^{-2/3}, \quad (7.128)$$

i.e. the magnetization parameter continuously decreases with radius until  $\sigma$  drops below unity at  $R_c$ . Beyond  $R_c$ ,  $\sigma$  continuously decreases as  $R_c/r$ .

In the rest of the discussion, we define the dynamics of Eq. (7.124) as the phase of *slow acceleration*.

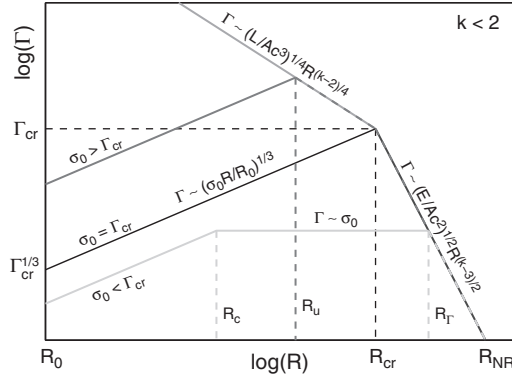


Figure 7.11

Evolution of the Lorentz factor of a Poynting-flux-dominated jet for different initial magnetization parameter  $\sigma_0$ . From Granot (2012).

When an ambient medium is considered, the dynamics of a Poynting-flux-dominated outflow depend on the comparison between the coasting radius  $R_c$  (which is essentially defined by  $\sigma_0$ ) and the jet deceleration radius  $R_{dec}$  (which is defined by the properties of both the jet (total energy and  $\sigma_0$ ) and the ambient medium). There are three possibilities (Granot 2012, see Fig. 7.11):

- If  $R_c < R_{dec}$ , the jet reaches the coasting Lorentz factor before deceleration;
- If  $R_c \sim R_{dec}$ , the jet immediately decelerates after reaching the maximum Lorentz factor;
- If  $R_c > R_{dec}$ , the jet decelerates before reaching the maximum Lorentz factor. The early deceleration phase has a shallower deceleration rate with  $\Gamma \propto r^{k-2}/4$ . Here  $k$  is the ambient density stratification parameter, i.e.  $n(r) \propto r^{-k}$ , so that  $\Gamma \propto r^{-1/2}$  for ISM ( $k = 0$ ), and  $\Gamma \sim \text{const}$  for wind ( $k = 2$ ). This mimics an energy injection phase of the blastwave evolution (see Chapter 8 for details).

### GRB Emission Site in a Poynting-Flux-Dominated Jet

Within a Poynting-flux-dominated jet, most energy is contained in the Poynting flux. To make efficient GRB prompt emission, most radiation energy must be converted from the original form of the Poynting flux energy.

Since the total energy available for radiation is only a fraction  $(1 + \sigma)^{-1}$  of the total wind energy,  $\sigma(R_{GRB})$  cannot be  $\gg 1$ . Three scenarios have been discussed in the literature.

The first scenario is that significant magnetic dissipation already occurs below the jet photosphere. Most of the magnetic energy is already converted to particle and radiation energy at small radii, so that one can have a relatively bright photosphere emission. The generalized magnetization factor  $\sigma$  (including the internal energy in the matter component) should be relatively low (say, not much greater than unity) at the photosphere radius. Many variants of this model have been discussed in the literature (e.g. Usov, 1994; Thompson, 1994; Giannios, 2006, 2008; Metzger et al., 2011). The difficulties of this group of models have been also discussed in the literature (e.g. Vurm et al., 2013; Asano and Mészáros, 2013; Kumar and Zhang, 2015; Bégué and Pe'er, 2015).

The second scenario is to keep the magnetic energy from dissipating until the jet reaches a large enough radius. Within this scenario,  $\sigma(R_{\text{ph}}) \gg 1$ , so that the photosphere emission is greatly suppressed (by a factor of  $(1 + \sigma(R_{\text{ph}}))^{-1}$ ). One plausible scenario of dissipating magnetic energy at a large radius from the central engine occurs through collisions among moderately high  $\sigma$  magnetic blobs (Zhang and Yan, 2011; Deng et al., 2015). These so-called ICMART (Internal-Collision-induced MAGnetic Reconnection and Turbulence) processes would bring down the local  $\sigma$  values in the flow through magnetic dissipation, directly converting the magnetic energy to radiation. In order to have efficient ICMART events,  $\sigma(R_{\text{ICMART}})$  before the event should be (moderately) greater than unity so that the outflow occurs during the “slow acceleration” phase. The ICMART processes dissipate magnetic energy rapidly, leading to an additional acceleration of the jet (Gao and Zhang, 2015).

The third scenario invokes an extremely high  $\sigma_0$ , with the Poynting flux dissipating only when the jet reaches the deceleration radius (Lyutikov and Blandford, 2003). The deceleration of the Poynting-flux-dominated jet triggers current instabilities within the jet, giving rise to a significant dissipation of the Poynting flux and powering GRB prompt emission. The GRB emission radius of this model is close to the deceleration radius, i.e.  $R_{\text{GRB}} \lesssim R_{\text{dec}}$ . One major difficulty of this scenario is to maintain an extremely high  $\sigma$  at  $R_{\text{dec}}$ , given all the possible channels of converting Poynting flux energy to other forms (kinetic, thermal, and radiation) before the jet reaches the deceleration radius (Fig. 7.5).

### 7.4.3 Characteristic Radii

Similar to §7.3.2, it is informative to summarize various characteristic radii for a Poynting-flux-dominated outflow with a duration  $\Delta t$  and an initial magnetization parameter  $\sigma_0 \gg 1$ .

- The central engine radius is  $R_0$ .
- The radius of causal disconnection, which is also the end of the rapid acceleration phase, is  $R_{\text{ra}} \sim c\Delta t$ . At this radius, one has  $\Gamma(R_{\text{ra}}) \simeq (1 + \sigma_0)^{1/3} \sim \sigma_0^{1/3}$ ,  $\sigma(R_{\text{ra}}) \simeq (1 + \sigma_0)^{2/3} \sim \sigma_0^{2/3}$ .
- The coasting radius is  $R_c = \sigma_0^2 R_{\text{ra}}$ . Between  $R_{\text{ra}}$  and  $R_c$  the shell accelerates as  $\Gamma \sim (\sigma_0 R / R_{\text{ra}})^{1/3}$  and  $(1 + \sigma)$  drops as  $\sim (1 + \sigma_0)^{2/3} (R / R_{\text{ra}})^{-1/3}$ . Above  $R_c$ ,  $\Gamma$  reaches the asymptotic value  $\sim (1 + \sigma_0)$ , and  $\sigma$  may continue to drop to below unity following  $\propto R_c / R$  (Granot et al., 2011).
- The deceleration radius is defined by the kinetic energy  $E / (1 + \sigma(R_{\text{dec}}))$ , where  $E$  is the total energy of the outflow and  $\sigma(R_{\text{dec}})$  is the magnetization parameter at the deceleration radius (Zhang and Kobayashi, 2005). If  $\sigma(R_{\text{dec}}) > 1$ , the initial deceleration index is shallow ( $\Gamma \propto r^{(k-2)/4}$ ), mimicking a blastwave with continuous energy injection (Zhang et al., 2006; Granot, 2012). The full deceleration radius is defined by the total  $E$ , beyond which the blastwave deceleration slope reaches the standard value from a constant energy case.
- The photosphere radius is defined by the thermal content of the outflow only. Assuming that a significant portion of the Poynting flux energy is converted to thermal energy below the photosphere (due to magnetic dissipation), the photosphere luminosity may

be characterized as  $L_{\text{ph}} \sim L_w/(1 + \sigma_{\text{ph}})$ , where  $\sigma_{\text{ph}}$  is the  $\sigma$  value at the photosphere radius. This luminosity can be used to define the photosphere radius. If no magnetic dissipation occurs, a pure Poynting-flux-dominated outflow has essentially no radiation field and the photospheric emission is greatly suppressed.

- If  $R_c < R_{\text{dec}}$ , hydrodynamic internal shocks may develop at  $R_{\text{IS}} > R_c$ , where  $\sigma(R_{\text{IS}}) < 1$ . These shocks dissipate kinetic energy and give rise to non-thermal emission. On the other hand, if internal shocks occur when at least one of the shells (usually the faster one) is still highly magnetized, i.e.  $\sigma(R_{\text{IS}}) \gg 1$ , without ICMART-like dissipation only a small fraction  $(1 + \sigma_{\text{IS}})^{-1}$  of total energy can be dissipated in internal shocks, so that these shocks are inefficient emitters.
- ICMART events require that the magnetic field lines of two colliding shells (blobs) have non-parallel field lines so that rapid magnetic reconnection can be triggered. For a helical magnetic geometry, a sudden discharge of magnetic energy may require multiple collisions (Zhang and Yan, 2011). For isolated magnetic blobs, the ICMART dissipation may occur immediately as the two blobs collide (Yuan and Zhang, 2012; Deng et al., 2015).
- If  $\sigma$  can remain  $\gg 1$  at the deceleration radius, current instability may be triggered at a radius close to the deceleration radius (Lyutikov and Blandford, 2003).

## 7.5 Hybrid Jet

As discussed in §7.2, a realistic central engine is likely hybrid. It includes a fireball component and a Poynting flux component.

The dynamical evolution of a hybrid jet is complicated and no detailed numerical simulations have been carried out to study it. Nonetheless, since thermal acceleration proceeds efficiently, one may speculate that the jet would first be accelerated thermally and then magnetically (Mészáros and Rees, 1997b). This was indeed confirmed by Vlahakis and Königl (2003) through a simplified analytical MHD model invoking both a thermal and a magnetic component.

Let us consider a hybrid central engine defined by two parameters, the fireball energy-to-mass ratio  $\eta$  and the initial generalized magnetization parameter  $\sigma_0$ . The dynamical evolution of the system may be delineated by the following toy model (Gao and Zhang, 2015).

First, the jet would undergo a *rapid acceleration* phase due to either thermal acceleration or magnetic acceleration. The relative importance between the two depends on the comparison between  $\eta$  and  $(1 + \sigma_0)^{1/2}$ .

If  $\eta > (1 + \sigma_0)^{1/2}$  is satisfied, after the thermal acceleration phase, the magnetized outflow has already reached the super-magneto-sonic regime, so that one has

$$\Gamma(R_{\text{ra}}) = \frac{\eta}{\Theta_{\text{ra}}}, \quad (7.129)$$

$$1 + \sigma(R_{\text{ra}}) = 1 + \sigma_0. \quad (7.130)$$

Notice that  $\sigma$  essentially does not decrease during this phase, but the matter portion of the luminosity changes from the thermal form to the kinetic form.

If  $\eta < (1 + \sigma_0)^{1/2}$  is satisfied, on the other hand, magnetic rapid acceleration can still proceed until the outflow Lorentz factor reaches the Alfvén Lorentz factor  $\gamma_A$ . One therefore has

$$\Gamma(R_{\text{ra}}) = \left[ \frac{\eta}{\Theta_{\text{ra}}} (1 + \sigma_0) \right]^{1/3}, \quad (7.131)$$

$$1 + \sigma(R_{\text{ra}}) = \left[ \frac{\eta}{\Theta_{\text{ra}}} (1 + \sigma_0) \right]^{2/3}. \quad (7.132)$$

Putting these together, one can generally define

$$\Gamma(R_{\text{ra}}) = \max \left( \frac{\eta}{\Theta_{\text{ra}}}, \left[ \frac{\eta}{\Theta_{\text{ra}}} (1 + \sigma_0) \right]^{1/3} \right), \quad (7.133)$$

$$1 + \sigma(R_{\text{ra}}) = \min \left( 1 + \sigma_0, \left[ \frac{\eta}{\Theta_{\text{ra}}} (1 + \sigma_0) \right]^{2/3} \right), \quad (7.134)$$

where  $\Theta_{\text{ra}} \sim 1$  is the total comoving energy per baryon at  $R_{\text{ra}}$ .

Beyond  $R_{\text{ra}}$  the jet would undergo a *slow acceleration* phase. Generally, one may define  $\Gamma \propto r^\delta$  with  $\delta \sim 1/3$ . Neglecting energy loss the flow would reach the maximum Lorentz factor

$$\Gamma_{\text{max}} = \eta(1 + \sigma_0) \quad (7.135)$$

at a coasting radius

$$R_c = R_{\text{ra}} \left( \frac{\Gamma_{\text{max}}}{\Gamma_{\text{ra}}} \right)^{1/\delta}. \quad (7.136)$$

The deceleration dynamics and the radius of GRB prompt emission of a hybrid jet are consistent with either the fireball model or the Poynting-flux-dominated model, depending on the values of  $(\eta, \sigma_0)$ . Figure 7.12 presents several examples of the dynamical evolution of hybrid jets with different initial conditions (Gao and Zhang, 2015).

## 7.6 A Scale Model

Since GRBs involve relativistic motions, the distance scales and time scales are not easy to comprehend from daily life experience. It is very useful to consider the following scale model in connection with our more familiar solar system.

Let us imagine that our Sun went off as a GRB.<sup>8</sup> Suppose that an observer at the outer edge of the solar system witnessed the launch and evolution of the GRB jet at a  $90^\circ$  angle. The following is what this observer would see.

<sup>8</sup> This would never happen since the mass of our Sun is too small to make core collapse in the far future.



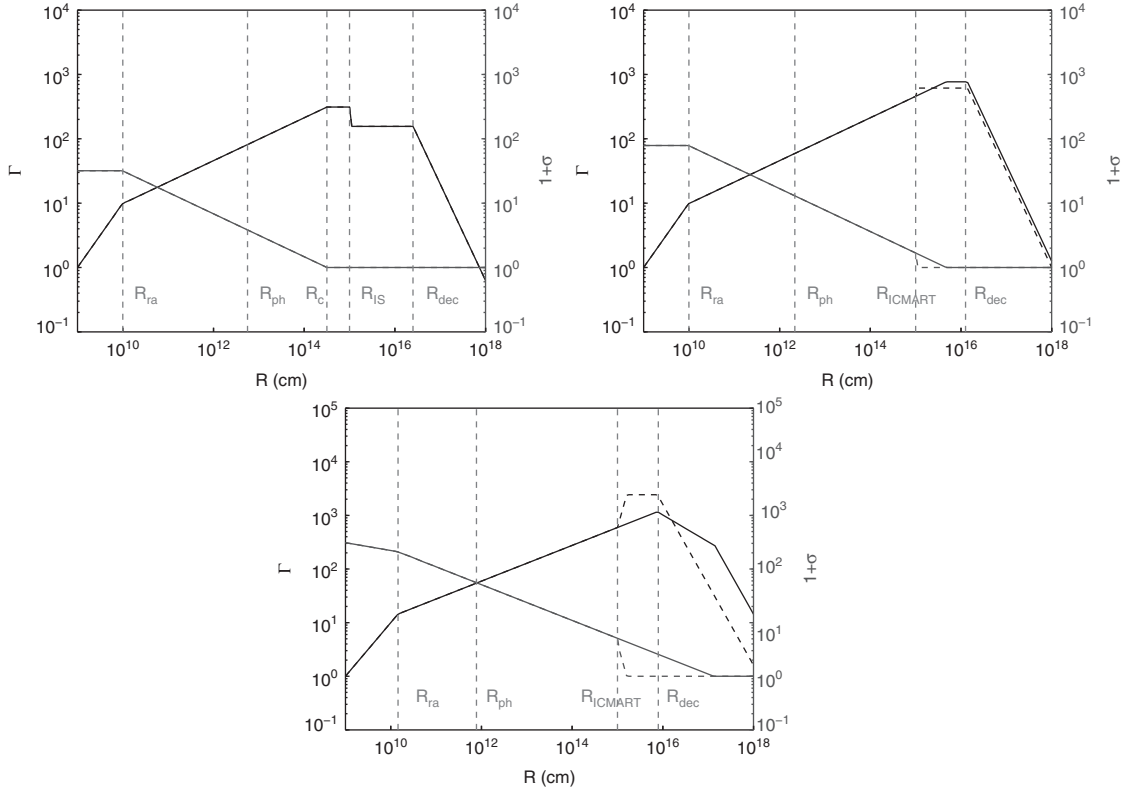


**Figure 7.12** The evolution of the Lorentz factor  $\Gamma$  (the initially rising curve) and the magnetization parameter  $(1 + \sigma)$  (the decreasing curve) of a hybrid jet for different initial conditions:  $(\eta, \sigma_0) = (10, 30), (10, 80), (10, 300)$ , respectively. From Gao and Zhang (2015).

- The size of a GRB Wolf–Rayet progenitor is typically  $R_* \sim 10^{11}$  cm. Since the radius of the Sun is  $R_\odot \simeq 7 \times 10^{10}$  cm, we may imagine that the size of the progenitor star is indeed the size of the Sun.
- At a certain epoch, core collapse occurs. A jet emerges from the surface of the Sun after about 10 seconds. After a brief acceleration phase, the head of the jet reaches a speed close to  $c$ . We further assume that the final Lorentz factor is 300, corresponding to  $v = 0.999994c$ .
- Let the engine last for 20 seconds. The length of the jet is therefore  $\sim 20$  light seconds ( $6 \times 10^{11}$  cm) in the lab frame, as measured by the  $90^\circ$  observer. So one can imagine a jet with length about  $20c/2R_\odot \sim 4$  times of the diameter of the Sun emerging from the surface of the Sun and traveling with the speed of light. Its length remains unchanged during propagation.
- Imagine a conical jet whose opening angle remains constant such that the cross section continuously increases with distance. Since the length of the jet remains constant, the jet is initially a flying “sword”, but gradually evolves into a “flying pancake” as the jet cross section continuously increases.

- About 1 minute later (0.0003 s according to the clock of an observer who looks down into the jet, i.e. a GRB observer) the jet reaches  $\sim 2 \times 10^{12}$  cm (1/3 of Mercury's semi-major axis) and the jet becomes transparent to photons in the direction of the GRB observer. Quasi-thermal photons are released at this photosphere radius.
- About 10 minutes to 3 hours later (0.003 s to 0.06 s for the GRB observer), the jet passes the orbits of Earth, Mars, Jupiter, Saturn, and Uranus. These are the radii where internal shocks develop.
- About 1 day later (0.5 s for the GRB observer), the jet passes through the Kuiper Belt (where Pluto, Eris, and other dwarf planets are located). This is roughly the distance of the envisaged ICMART processes if the outflow is sufficiently magnetized.
- About 1 month later (14 s for the GRB observer), the jet reaches close to the radius of the "Oort Cloud" for comets. This is the radius where the jet starts to decelerate.
- About 1 year later (1 yr for the GRB observer also), the fireball reaches about 1/4 the distance to Proxima Centauri (our nearest-neighbor star system). The blastwave is sufficiently decelerated and enters the non-relativistic phase.

## 7.7 Alternative Ideas

Besides the mainstream theoretical framework discussed above, in the literature there are several alternative ideas proposed to interpret the GRB phenomenology. In the following we briefly summarize and critically comment on these models.

### 7.7.1 Cannonball

In a series of papers, Dar, De Rújula, and Dado suggested that GRBs are relativistic "cannonballs" ejected from central black holes. This model is summarized in a review article by Dar and de Rújula (2004).

The common ingredients that the cannonball model shares with the mainstream models include:

- The progenitor is a massive star that undergoes core collapse and gives rise to a supernova;
- The ejecta moves with a relativistic speed towards the direction of the observer;
- A compact central engine with an accretion disk or torus is envisaged to launch the ejecta;
- Synchrotron radiation of electrons accelerated during the deceleration of the ejecta gives rise to the observed afterglow.

The following ingredients of the model are significantly different from the mainstream models:

- The ejecta is not treated as a fluid, but rather a "cannonball", which essentially holds its size without significant expansion during its propagation in the ISM. In this scenario,

neither sound waves nor shock waves are envisaged to propagate inside the cannonball, which may not be easy to justify for a relativistically moving gaseous outflow.

- Due to the small size of the cannonballs, in most configurations, the ejecta does not beam squarely towards Earth. The line of sight is usually outside the  $1/\Gamma$  cone extended by the cannonball, but is still close to the direction of bulk motion. The geometry of the system is more analogous to that of blazars or micro-quasars. The radio afterglow observations of GRB 030329 with VLBA by Taylor et al. (2004) led to measurement of the expansion of the afterglow source from 25 days ( $\sim 0.07$  mas) to 83 days ( $\sim 0.17$  mas) after the burst, with an apparent expansion speed  $3\text{--}5c$ . This is consistent with the mainstream fireball model of GRBs but is not consistent with the cannonball model.
- The radiation mechanism of GRB prompt emission is inverse Compton scattering in the cannonball model. Electrons are from the cannonball, and target photons are from either the supernova or the ambient light dubbed “glory”, which is the trapped light (or echo) emitted by the progenitor before explosion.
- The acceleration of electrons from the ambient medium does not occur through shocks, but through bulk collision off the cannonball. The cannonball is treated as a rigid body. Again, it is difficult to circumvent shock formation for two colliding fluids. Even if one may argue that no shock may propagate into the cannonball itself (for example, if it is highly magnetized), it is still impossible to avoid the forward shock that propagates into the ISM given that the cannonball speed greatly exceeds the sound speed of the ISM.

### 7.7.2 Fireshell

Over the years, Ruffini and colleagues advocated the “fireshell” model of GRBs. This model is summarized in a review article by Ruffini et al. (2008).

The common ingredients that the fireshell model shares with the mainstream models include:

- The ejecta moves with a relativistic speed towards the observer;
- The central engine is a newborn black hole;
- Afterglow is produced by the interaction between the fireshell and the ambient medium.

The following ingredients of the model are significantly different from the mainstream models:

- The central engine black hole is “naked”. No accretion is required. Rather, vacuum polarization in a Kerr–Newman (charged, rapidly spinning) black hole is envisaged to discharge energy of the order  $10^{54}$  erg. This ejection is likely impulsive, without extended central engine activity.
- The ejection is essentially isotropic and, hence, the ejecta is in the form of a “fireshell”. It is unclear how rich phenomenology invoking jet breaks may be interpreted within this model.

- Since no extended central engine activity is envisaged, only one pulse in the observed GRB lightcurves can be interpreted as the direct emission from the fireshell. This is called the “prompt-GRB” or “P-GRB”. Usually this is taken as the first pulse in the lightcurves. All the other pulses are interpreted as the “afterglow-GRB” or “A-GRB”. In order to account for significant variability observed in the prompt emission lightcurves, the authors assumed that the immediate medium around the black hole is extremely clumpy. Each interaction with these clumps produces a pulse in the lightcurve.
- The radiation mechanism of all episodes is essentially thermal. The “P-GRB” is essentially the photosphere emission within the mainstream models. No shock formation or synchrotron radiation have been discussed in the fireshell models, and the “A-GRB” emission is also regarded as thermal emission. No interpretation of the broad-band afterglow is available within the model.
- The difference between long and short GRBs is whether the “P-GRB” is much brighter than the “A-GRB”. This is connected to the baryon loading of the fireshell, with short GRBs being cleaner.
- Long GRBs are envisaged to be produced in binary systems with the explosion of the primary inducing the gravitational collapse of a secondary neutron star (the Induced Gravitational Collapse, or IGC, model). This could interpret the association of Type Ic SNe with long GRBs. Ruffini et al. (2016, 2018) extended the analysis by hypothesizing eight sub-categories of binary progenitor systems to interpret long and short GRBs with a variety of luminosities.

### 7.7.3 Precession

Many authors from different groups have suggested that central engine jet precession plays an important role in accounting for GRB phenomenology (e.g. Lei et al., 2007; Romero et al., 2010; Liu et al., 2010; Fargion, 2012). The lack of apparent quasi-periodic signals in the majority of GRBs suggests that the precession effect, if relevant, may not be the main mechanism for interpreting the diverse phenomenology in the majority of GRBs.

## Exercises

- 7.1 A long GRB at  $z = 2.83$  was detected by both *Swift* and *Fermi* LAT. The total fluence in the 10–1000 keV band is  $(2.22 \pm 0.01) \times 10^{-5} \text{ erg cm}^{-2}$ . The detected minimum variability time scale in the lightcurve is  $\sim 1$  s. One 2 GeV photon was detected by LAT during the prompt emission phase. Derive a lower limit of the bulk Lorentz factor  $\Gamma$  assuming the internal shock model. Its early optical afterglow lightcurve shows a peak around 65 s after the GRB trigger, and the lightcurve behavior is consistent with the external forward shock model in an ISM medium. Estimate  $\Gamma$  using the optical data. Compare the two constraints.
- 7.2 Derive Eqs. (7.31)–(7.33) and subsequent fireball evolution based on the basic relativistic hydrodynamical conservation equations, Eqs. (4.9)–(4.11).

- 7.3 Derive the fireball photosphere scaling properties in Eqs. (7.71)–(7.74).
- 7.4 Derive the deceleration radius, time, and  $\Gamma_{\text{dec}}$  for both ISM and wind cases. Prove the numerical factors 0.9 in Eq. (7.80) and 1.3 in Eq. (7.86).
- 7.5 Derive the Sedov radius for both the constant density ISM model and the wind model.